Influence of Local Water Vapor Analysis Uncertainty on Ensemble Forecasts of Tropical Cyclogenesis Using Hurricane Irma (2017) as a Testbed

CHRISTOPHER M. HARTMAN,[a] FALKO JUDT,[b] AND XINGCHAO CHEN[a]

[a] *Department of Meteorology and Atmospheric Science, and Center for Advanced Data Assimilation and Predictability Techniques, The Pennsylvania State University, University Park, Pennsylvania*
[b] *National Center for Atmospheric Research, Boulder, Colorado*

(Manuscript received 1 September 2023, in final form 7 March 2024, accepted 15 March 2024)

ABSTRACT: Tropical cyclone formation is known to require abundant water vapor in the lower to middle troposphere within the incipient disturbance. In this study, we assess the impacts of local water vapor analysis uncertainty on the predictability of the formation of Hurricane Irma (2017). To this end, we reduce the magnitude of the incipient disturbance's water vapor perturbations obtained from an ensemble-based data assimilation system that constrained moisture by assimilating all-sky infrared and microwave radiances. Five-day ensemble forecasts are initialized two days before genesis using each set of modified analysis perturbations. Growth of convective differences and intensity uncertainty are evaluated for each ensemble forecast. We observe that when initializing an ensemble forecast with only moisture uncertainty within the incipient disturbance, the resulting intensity uncertainty at every lead time exceeds half that of an ensemble containing initial perturbations to all variables throughout the domain. Although ensembles with different initial moisture uncertainty amplitudes reveal a similar pathway to genesis, uncertainty in genesis timing varies substantially across ensembles since moister members exhibit earlier spinup of the low-level vortex. These differences in genesis timing are traced back to the first 6–12 h of integration, when differences in the position and intensity of mesoscale convective systems across ensemble members develop more quickly with greater initial moisture uncertainty. In addition, the rapid growth of intensity uncertainty may be greatly modulated by the diurnal cycle. Ultimately, this study underscores the importance of targeting the incipient disturbance with high spatiotemporal water vapor observations for ingestion into data assimilation systems.

SIGNIFICANCE STATEMENT: Hurricanes form from clusters of thunderstorms that organize into a coherent system. One of the key ingredients for the formation process is an abundance of moisture. In this study, we test the sensitivity of hurricane formation to the initial moisture content in the vicinity of the cluster of thunderstorms that would become Hurricane Irma (2017). To do so, we initialize sets of forecasts each having a different variability of initial moisture content within the embryonic disturbance. Our results show that the predictability of hurricane formation is highly dependent on the uncertainty of the moisture content within the initial disturbance. Consequently, more high-quality observations of the moisture within the precursor disturbances to hurricanes are expected to improve forecasts of their formation.

KEYWORDS: Tropical cyclones; Data assimilation; Numerical weather prediction/forecasting

1. Introduction

Tropical cyclogenesis, the formation of a tropical cyclone (TC), is the most challenging stage in the life cycle of a TC to predict (Emanuel 2018). More than a decade ago, it was revealed that TC genesis forecasts had improved due to numerical modeling and data assimilation (DA) innovations (Halperin et al. 2013). Despite this progress, accurate TC genesis forecasts remain limited by highly nonlinear multiscale interactions involving moist convective processes (Emanuel 2018; Tang et al. 2020; Núñez Ocasio 2021). This begs the question of how much TC genesis forecasts can be further improved in the future given their dependence on moist convection.

Both observational studies (e.g., Smith and Montgomery 2012; Komaromi 2013) and modeling studies (e.g., Sippel and Zhang 2008; Zhang and Sippel 2009; Sippel and Zhang 2010; Torn 2010; Sippel et al. 2011; Doyle et al. 2012; Torn and Cook 2013; Poterjoy and Zhang 2014a; Komaromi and Majumdar 2015) have revealed that TC genesis is sensitive to the moisture both within the incipient disturbance and in the environment through which it is moving. When moist convection and its associated latent heating happen to occur in the same areas as low-level vorticity maxima, vortex stretching can create rotating plumes of deep convection known as vortical hot towers (VHTs; Hendricks et al. 2004; Montgomery et al. 2006). These VHTs chaotically interact with one another, oftentimes merging. The collective influence of the VHT updrafts, through the low-level convergence they produce, is believed to help spin up the low-level vortex, thereby leading to TC genesis. From a larger-scale perspective, there is a growing body of research demonstrating that moist convection present within the trough of an African easterly wave (AEW) can not only enhance the AEW vortex (Hall et al. 2006; Berry and Thorncroft 2012; Russell and Aiyyer 2020; Russell et al. 2020) but also make the AEW more favorable for genesis by impacting the distribution of moisture and future convection (Wang et al. 2010; Hopsch et al. 2010; Berry and Thorncroft 2012; Peng et al. 2012;

Corresponding author: Xingchao Chen, xzc55@psu.edu

DOI: 10.1175/MWR-D-23-0195.1

Leppert et al. 2013a,b; Brammer and Thorncroft 2015; Brammer et al. 2018; Núñez Ocasio et al. 2020, 2021). Recent studies have also indicated that TC genesis might be more likely shortly after an AEW interacts with a convectively coupled Kelvin wave in its active phase because both moisture and convective coverage are increased (Ventrice et al. 2012a,b; Schreck 2015, 2016; Lawton et al. 2022; Lawton and Majumdar 2023). Based on these studies, the impact of moisture and deep convection on the predictability of TC genesis cannot be understated.

In studying TCs that originate from AEWs, it is common to analyze the evolution of convection in a frame of reference moving with the wave. In this frame of reference, the preferred location of TC genesis is hypothesized to occur at the center of a meso-α-scale (i.e., 200–2000 km) region of closed lower-tropospheric AEW-relative streamlines (Dunkerton et al. 2009). The center of this pouch is referred to as the sweet spot. Found at the intersection of the wave trough and its critical layer (i.e., where the wave-relative zonal wind is zero), the sweet spot serves as a focal point for the aggregation of convection within a region of maximal relative vorticity and minimal strain/shearing deformation. In the absence of strong shear, the sweet spot is hypothesized to be largely protected by the pouch from potentially damaging dry air intrusions. Furthermore, since the air within the pouch is continuously recirculated, the sweet spot typically has an abundance of moisture. Consequently, the area containing the sweet spot serves as an ideal location for the formation and aggregation of VHTs. The marsupial pouch paradigm described heretofore has been supported and reinforced by both modeling studies (e.g., Wang et al. 2010; Li and Pu 2014; Asaadi et al. 2016, 2017; Rajasree et al. 2016a,b) and field campaigns, including the Tropical Cyclone Structure 2008 (TCS-08) field experiment (Montgomery et al. 2010a), the Pre-Depression Investigation of Cloud-Systems in the Tropics (PREDICT; Montgomery et al. 2012), and NASA's Genesis and Rapid Intensification Processes (GRIP) field experiment (Braun et al. 2013). In short, the preferred location of TC genesis, in a wave-relative sense, is hypothesized to be near the intersection of the trough and critical layer of an AEW.

By using an AEW-relative framework for analysis, a recent study by Hartman et al. (2023) showed the improvements that can be brought to the timing of TC genesis forecasts by better capturing the convective evolution within the pouch region during the early hours of integration. That study (hereafter referred to as "HCC23") used an ensemble-based DA system to assimilate all-sky infrared (IR) radiances [hereafter brightness temperatures (BTs)] from a geostationary satellite. Through the assimilation of those BTs, the initial moisture content within the pouch and environment was modulated (in this scenario decreased; see Fig. 10 of HCC23) such that deterministic forecasts exhibited a more realistic convective evolution and genesis timing compared to an experiment that withheld them.

Motivated by the results of HCC23, this study seeks to shed light on how much improvement can be brought to the timing of TC genesis in forecasts by reducing errors in the initial moisture content within the pouch region. We stress that this study differs from HCC23 in that it is focused entirely on the impacts of local initial water vapor uncertainty on the predictability of TC genesis. To demonstrate the sensitivity of genesis forecasts to the initial moisture content within the pouch, we conduct sets of ensemble forecasts differing only in the amplitude of the initial moisture perturbations within it. As in HCC23, we use Hurricane Irma (2017) as a test case. For a brief meteorological history of the storm, the interested reader is referred to section 2 of HCC23 as well as the National Hurricane Center's (NHC's) Tropical Cyclone Report (Cangialosi et al. 2018).

This paper is organized as follows. Section 2 describes the DA system used to generate the initial ensemble for this study, as well as the method by which the initial moisture was modified within it. Section 3 presents the results of the moisture modification ensemble forecasts. Finally, section 4 provides a discussion of the results, including questions that remain.

2. Methodology

In this section, we describe the DA system used to generate the initial ensemble of analyses for this study. After that, we detail the observations assimilated by the DA system. Finally, we explain the method by which the moisture of the initial ensemble was modified.

a. DA and forecast system

An initial 60-member ensemble of analyses for this study is provided by the Pennsylvania State University Weather Research and Forecasting Model with ensemble Kalman filter (PSU WRF-EnKF) DA system (Zhang et al. 2009, 2011, 2016; Weng and Zhang 2012, 2016; Chen and Zhang 2019a; Zhang et al. 2019). To generate the ensemble, perturbations are applied to the National Centers for Environmental Prediction's (NCEP) Global Forecast System (GFS) analysis using WRFDA's CV3 background error covariance option (Barker et al. 2004). This ensemble is then "spun up" for 12 h using the Advanced Research version of the WRF Model, version 3.6.1 (Skamarock et al. 2008), to develop flow-dependent ensemble statistics before the first DA cycle. The DA component of this system follows the ensemble square root filter formulation of Whitaker and Hamill (2002), which updates the state via ensemble correlations that exist between simulated observations and state variables. During the assimilation of all-sky IR or microwave (MW) BTs, the Community Radiative Transfer Model (CRTM; Han et al. 2006, 2007; Weng 2007) is used as the observation operator that generates the simulated BTs. After assimilation, the ensemble of analyses is then integrated into the next DA cycle by the WRF model. To maintain sufficient ensemble spread during the DA cycling, relaxation to prior perturbations (Zhang et al. 2004) with a coefficient of 80% is applied. In other words, the final ensemble perturbations at each DA cycle are a mixture of 20% of the posterior perturbations and 80% of the prior perturbations.

The size and location of the domain for this study are indicated by the rectangle in Fig. 1a. This domain size maintains sufficient distance between its boundaries and the disturbance of interest during all times of the DA cycling and subsequent forecasts. In the vertical direction, there are 43 levels with a top

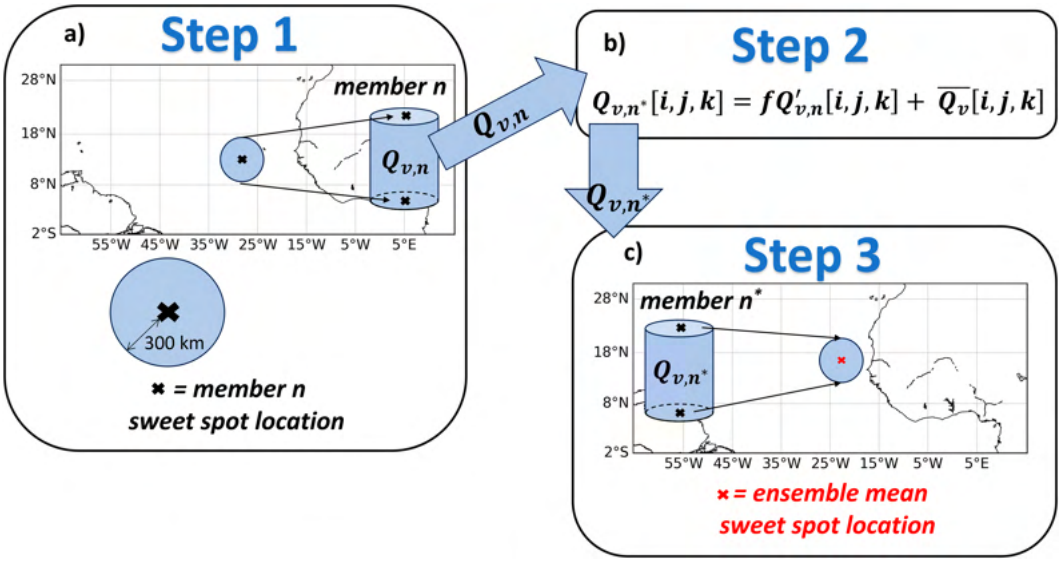

FIG. 1. Schematic diagram showing the method by which each PRIMER ensemble is generated in this study. (a) Step 1: The sweet spot locations of each of the n members in the PSU WRF-EnKF analysis are identified. The QVAPOR of each member ($Q_{v,n}$) is then extracted within a cylinder of radius 300 km surrounding its respective sweet spot. (b) Step 2: Using pouch-relative coordinates (i.e., the sweet spot for each member is the central axis of its cylinder), new QVAPOR values for each member (Q_{v,n^*}) are calculated within the cylinders by rescaling the perturbations from the ensemble mean by a factor f and then adding back the ensemble mean. (c) Step 3: The new PRIMER ensemble is generated by inserting each of the n modified cylinders into the grid of the PSU WRF-EnKF analysis mean such that their axes are collocated with the central axis of the analysis mean sweet spot location. The result is an n member ensemble having differences in only the QVAPOR within 300 km of the ensemble mean sweet spot location.

at 10 hPa. Due to the number of ensemble forecasts in this study, combined with the size of the regional domain needed, computational constraints limit us to using a single, stationary 9-km domain.

Several parameterization schemes are used during both the forecast step of the DA cycling and the ensemble forecasts. These include the following: the Thompson double-moment microphysics scheme (Thompson et al. 2008), the Yonsei University planetary boundary layer scheme (Hong et al. 2006), and the Rapid Radiative Transfer Model (RRTM) longwave and shortwave radiation schemes (Iacono et al. 2008). Surface fluxes of momentum and sensible and latent heat are parameterized via the method of Green and Zhang (2013). Since the grid spacing in this study has been shown to sufficiently resolve the main physical processes involved in TC genesis (e.g., Montgomery et al. 2010b), as well as the maintenance of mesoscale convective systems (MCSs) without the need for cumulus parameterization (e.g., He et al. 2019; Wang et al. 2015; Ying and Zhang 2018; Zhang et al. 2017; Chen et al. 2018a,b; Chen and Zhang 2019b; Ying and Zhang 2017; Chan et al. 2020; Ou et al. 2020; Chen et al. 2021; Chan and Chen 2022; Chen et al. 2022a,b), we do not use a cumulus parameterization scheme.

b. *Observations assimilated*

Observations that we assimilate during hourly DA cycling fall into three categories: 1) surface- and upper-level observations from the World Meteorological Organization's (WMO's) Global Telecommunication System (GTS), 2) all-sky IR BTs observed by the upper-tropospheric water vapor channel (channel 5) of the SEVIRI instrument on board the *Meteosat-10* satellite, and 3) all-sky MW BTs from NASA's Global Precipitation Measurement (GPM) mission network of satellites (Hou et al. 2014; Skofronick-Jackson et al. 2017). Ensemble covariances were localized using the Gaspari and Cohn (1999) fifth-order piecewise polynomial to eliminate the effects of spurious long-distance correlations. Following HCC23, the localization radius of influence (ROI) used in the horizontal direction was 300 km for surface GTS observations, 100 km for upper-air GTS observations, and 100 km for all-sky IR BTs. For more details about quality control, data thinning, and localization, we refer the interested reader to section 3c of HCC23.

This study supplements the hourly assimilation of all-sky IR BTs with all-sky MW BTs. We assimilate one low-frequency channel (19 GHz vertically polarized) and one high-frequency channel (183.31 ± 6.6 GHz; 89 GHz for sensors not having 183 GHz) to be consistent with Table B1 of Zhang et al. (2021). After thinning MW observations to a separation of 27 km (comparable to the IR BTs), an average of 400 low-frequency observations are assimilated in 8 of the 12 DA cycles and an average of 800 high-frequency observations are assimilated in 10 of the 12 DA cycles within 1000 km of the sweet spot location that one would identify if they used the ERA5 zonal (U) and meridional (V) winds at 850 hPa. To be consistent with the assimilation of IR BTs, ensemble covariances when assimilating MW BTs are localized in the horizontal direction with a radius of influence of

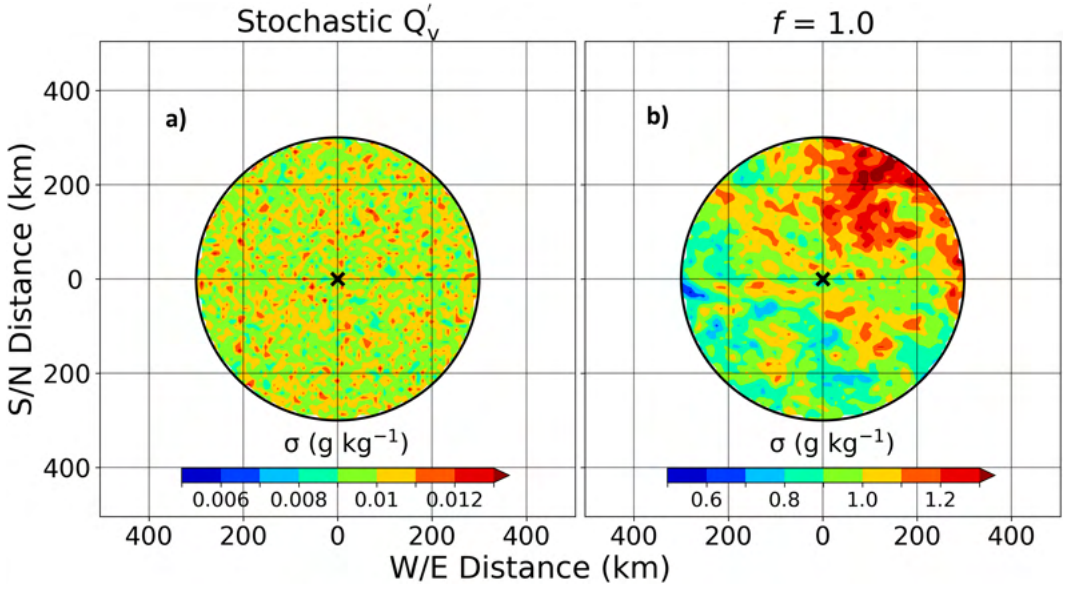

FIG. 2. Initial-hour ensemble spread of the QVAPOR (g kg^{-1}) at the lowest model level for the (a) stochastic Q_v', and (b) PRIMER-1.0 ensemble forecasts. In each subplot, the black "x" denotes the sweet spot location. Note that the color bars are different for each subplot.

100 km for all variables. As with the assimilation of IR BTs, we employ the adaptive observation error inflation (Minamide and Zhang 2017) method to adaptively inflate the observation error when large mismatches occur between observed and simulated cloud scenes. Consequently, none of the thinned MW BTs are rejected during the assimilation process. Finally, when calculating simulated MW BTs, we use nonspherical ice hydrometeor scattering properties developed by Sieron et al. (2017, 2018) to be consistent with the microphysics parameterization scheme.

c. *Moisture modification ensembles*

In this subsection, we describe the method by which the initial ensemble of analyses (i.e., the analyses provided by the DA system) is modified to produce new sets of ensembles (to be described shortly). Since the goal is to see the impact of initial moisture uncertainty within the pouch region on the predictability of tropical cyclogenesis, we generate ensembles that differ only in the moisture content within the pouch region at initialization time. More specifically, the uncertainty of the initial moisture content varies systematically from ensemble to ensemble. To accomplish this, we shrink the water vapor mixing ratio (hereafter QVAPOR) perturbations of the original ensemble while keeping the ensemble mean and spatial pattern of moisture unchanged. This process is performed in a pouch-relative sense, since each ensemble member has a different sweet spot location in the original ensemble. We refer to this new set of ensembles as the Pouch-Relative Initial Moisture Ensemble-Perturbation Reduction (PRIMER) ensembles.

Figure 1 outlines the three steps we follow to generate the PRIMER ensembles. The first step in this figure shows the extraction of the QVAPOR values within a cylinder of radius 300 km centered on the initial sweet spot location of each member. These extracted cylinders are then aligned such that their central axes are collocated and each grid point within these cylinders is aligned based on its position relative to the central axis. In other words, we work in sweet-spot-relative coordinates such that the sweet spot is the origin/central axis. In the second step, the perturbations from the mean are shrunk at each grid point within the cylinders by rescaling them by a fraction f and then adding them back to the ensemble mean value at that grid point. For the third step, we identify the sweet spot location of the PSU WRF-EnKF analysis mean and replace the QVAPOR values within 300 km of it with the values obtained in step 2. This results in new ensembles, with the only difference across members being the QVAPOR within 300 km of the ensemble mean sweet spot location. It is important to note that all variables other than QVAPOR are set to the ensemble mean values at every location within the domain. Also, the QVAPOR values outside of the cylinders are set to the ensemble mean values. Finally, the boundary conditions for all forecasts come from the NCEP GFS analysis of 0000 UTC 28 August. This design enables us to isolate the impacts of initial moisture uncertainty within the pouch region, disentangling it from other sources of uncertainty such as environmental moisture and other variables.

A total of 12 moisture modification ensembles are produced—11 PRIMER ensembles plus stochastic Q_v'. In stochastic Q_v', random perturbations drawn from a normal distribution ($\mu = 0$, $\sigma = 0.01$ g kg^{-1}) are added to the ensemble mean QVAPOR values at only the lowest model level within 300 km of the ensemble mean sweet spot location. This ensemble is created to show the intrinsic limit of predictability for this case. The 11 PRIMER ensembles (PRIMER-0.01, PRIMER-0.1, PRIMER-0.2, …, PRIMER-1.0) differ only in the fraction f by which the QVAPOR perturbations are rescaled. Figure 2 shows the initial-hour ensemble spread (i.e.,

standard deviation) of the lowest model level QVAPOR for two of the ensembles. Note the spread of stochastic Q'_v (Fig. 2a) is two orders of magnitude lower than PRIMER-1.0, which has the highest perturbation amplitude (Fig. 2b). By design, the spatial pattern of QVAPOR spread for PRIMER-1.0 is identical to the other ten PRIMER ensembles (not shown). Consequently, the spread of PRIMER-0.01 is similar in magnitude to stochastic Q'_v but has a spatial pattern identical to the other PRIMER ensembles. The spatial pattern of QVAPOR spread in the PRIMER ensembles (Fig. 2b) reveals the pattern of inner-pouch moisture uncertainty that exists in this state-of-the-art DA system. Moisture uncertainty is greatest in the northeast quadrant of the pouch and generally decreases toward the southwest. This pattern of moisture uncertainty results from uncertainty in the positioning of a moisture gradient that exists to the northeast of each member's pouch combined with uncertainty in the positioning of those pouches (not shown).

3. Results

This section is divided into three subsections. In the first subsection, we present the results of the 5-day ensemble forecasts and quantify the impact of initial moisture uncertainty on the evolution of intensity uncertainty. In the second subsection, we show the impact of initial moisture uncertainty on the growth of convective differences during the early hours of the forecasts. Finally, the last subsection reveals the impact of initial moisture uncertainty on pathways to genesis and the timing of genesis.

a. Impact of initial moisture uncertainty on intensity uncertainty

The initial ensemble containing the full EnKF perturbations that we use in this study comes from the 0200 UTC 28 August analysis (the ninth DA cycle) of the PSU WRF-EnKF. This analysis is chosen because the ensemble mean of the ensemble forecast initialized from it follows the NHC's HURDAT2 best track data more closely than any other ensemble initialized around 48 h before the observed genesis time. Note that in this study, we define the observed genesis time as the time at which Irma entered the best track database as a tropical depression (i.e., 0000 UTC 30 August).

Before exploring the growth of intensity uncertainty in the PRIMER ensembles, it is important to keep in mind the intensity uncertainty that exists in the full EnKF ensemble, which serves as the benchmark for this study. Figure 3 shows the temporal evolution of the intensity and track of each member in the full EnKF ensemble, which was initialized 46 h before the observed genesis time. Throughout this manuscript, we use the term "storm center" to refer to the sweet spot location prior to genesis time and the TC center location after genesis time. The TC center location is determined using the tracking algorithm of HCC23, which is loosely based on the study of Majumdar and Torn (2014) in that we use the same quantities. This algorithm defines the TC center as the centroid of the triangle having vertices at the locations of the maximum 700–850-hPa layer-averaged circulation, maximum 200–850-hPa thickness anomaly, and minimum sea level pressure (SLP). A quick look at Fig. 3a reveals the wide range of

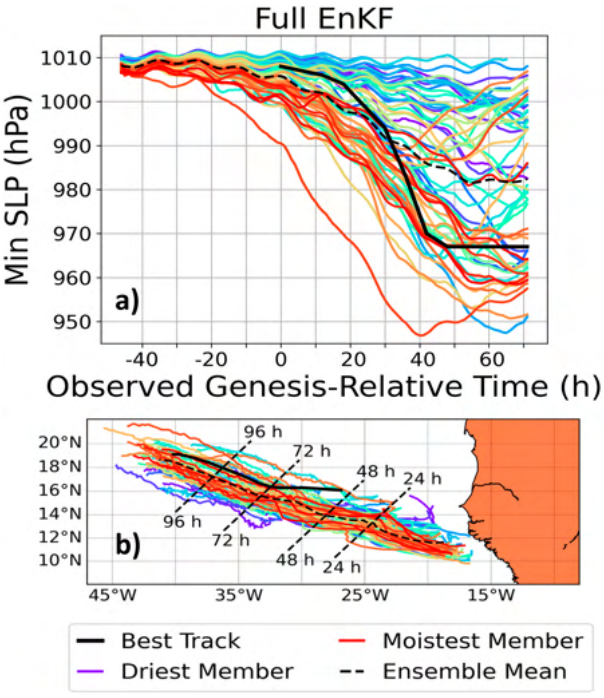

FIG. 3. Forecasts of the (a) minimum SLP (hPa) within 300 km of the storm center and (b) track of the disturbance for the ensemble initialized with the full PSU WRF-EnKF perturbations to all variables. Line colors represent the amount of moisture within 300 km of the pouch center at initialization time, with the coolest colors having the lowest volume-averaged QVAPOR and the warmest colors having the highest volume-averaged QVAPOR. The position of the ensemble mean forecasted storm center at select lead times is indicated in (b) by orthogonal black dashed lines.

intensity forecasts in the full EnKF ensemble. By the observed genesis time, the range of minimum SLP values reaches 10–20 hPa and grows to ~60 hPa by the end of the forecasts. Although the ensemble mean captures the genesis and subsequent intensification (from 0 to 40 h) of Irma quite well compared to the best track, many members do not—some drastically overestimate the intensity, while others fail to develop it at all. Furthermore, there is a general tendency to produce a stronger storm when the initial moisture content within the pouch is higher. This tendency is more noticeable during the pregenesis period. The full EnKF also exhibits sizeable track uncertainty (Fig. 3b). This uncertainty is a result of several factors. These factors include uncertainty in the initial sweet spot location, uncertainty in the initial values of all variables, the β effect (i.e., a northwestward drift of the vortex *in the Northern Hemisphere* due to differential advection of Earth's vorticity that increases with increasing vortex strength), and nonlinear interactions among variables during integration. In summary, the benchmark for this study presents us with ensemble forecasts that, although representative of a state-of-the-art DA system, have considerable room for improvement in both intensity and track.

Now that we have shown the full range of intensities in the full EnKF ensemble, we turn to the intensity uncertainty that

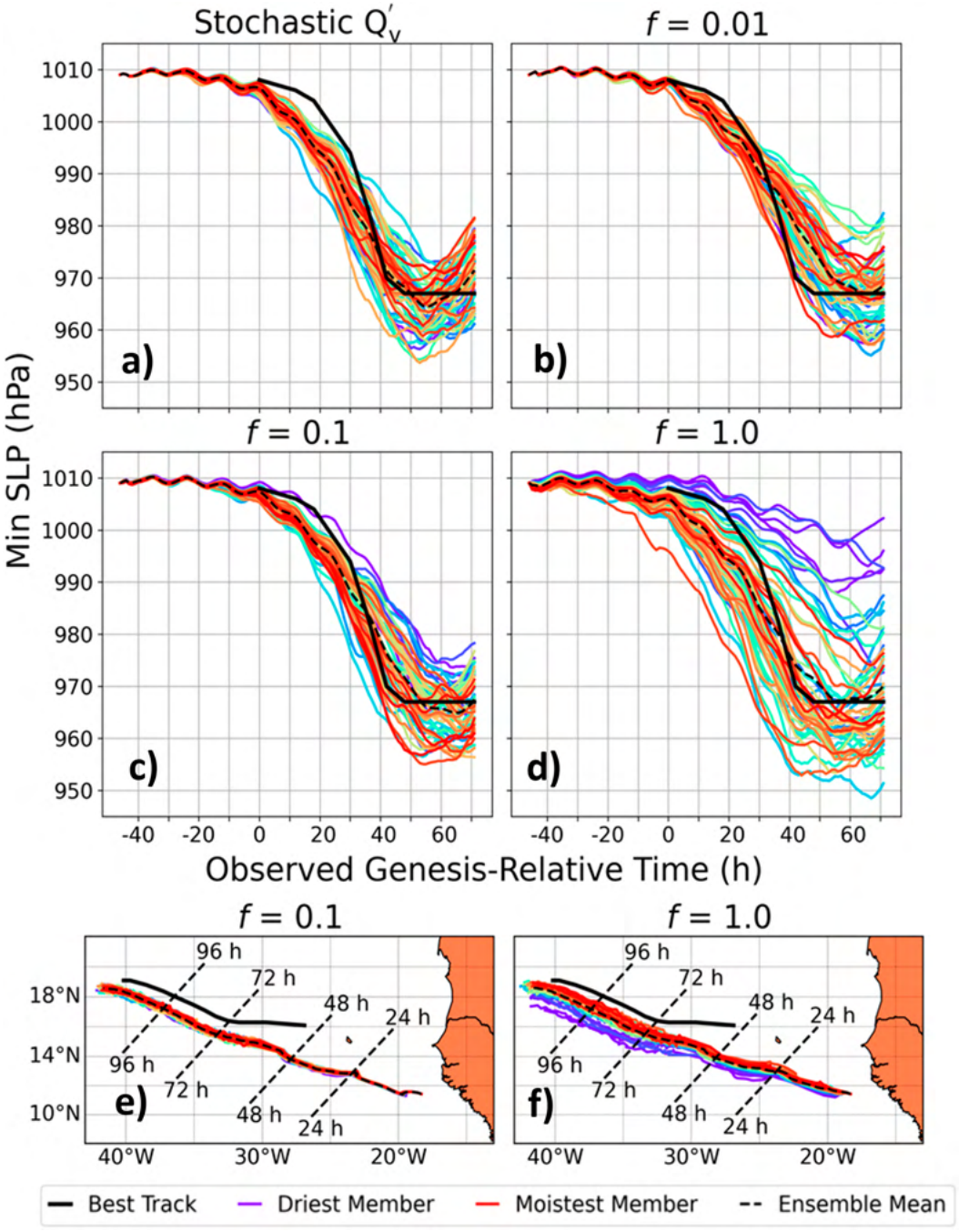

FIG. 4. As in Fig. 3, but for forecasts initialized with (a) stochastic perturbations to the lowest model level QVAPOR, as well as (b) PRIMER-0.01, (c),(e) PRIMER-0.1, and (d),(f) PRIMER-1.0 perturbations. Track forecasts for the stochastic and PRIMER-0.01 ensembles exhibit insufficient spread to warrant inclusion.

develops because of the initial moisture uncertainty within the pouch. Figure 4 shows the intensity and track forecasts for some of the moisture modification ensembles. In terms of minimum SLP, the stochastic Q_v' (Fig. 4a) and PRIMER-0.01 (Fig. 4b) ensemble forecasts are visually quite similar. Differences that arise between the intensities of these two ensembles, albeit quite small, might be a result of the spatial pattern of initial QVAPOR uncertainty. How the spatial pattern of initial QVAPOR uncertainty impacts the intensity uncertainty is an interesting question but is beyond the scope of this study. Nevertheless, two additional ensemble forecasts, each using the PRIMER-1.0 QVAPOR perturbations but rotated clockwise by 90° and 180°, were integrated to see whether the main results of this study might be impacted by

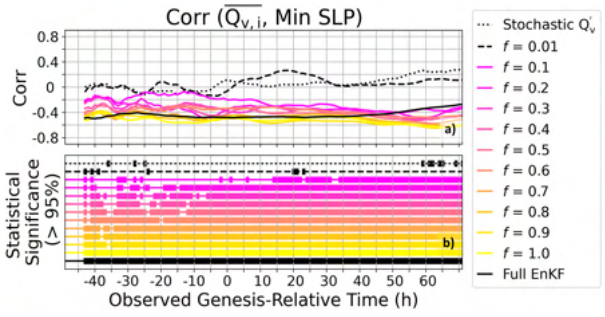

FIG. 5. (a) Pearson's correlation coefficient between the initial-hour volume-averaged QVAPOR within 300 km of the pouch center and the minimum SLP within 300 km of the storm center for each ensemble forecast. The times for which each correlation value in (a) is statistically significant at greater than 95% confidence based on the Student's two-tailed t test (Gosset 1908) are indicated in (b).

the spatial pattern of initial QVAPOR uncertainty. The temporal evolution of intensity uncertainty in these two extra ensembles closely matched that of the original PRIMER-1.0 ensemble (figure not shown), indicating that the spatial pattern of initial QVAPOR uncertainty should not play a significant impact on the results herein. As initial QVAPOR uncertainty increases to one-tenth (PRIMER-0.1; Fig. 4c) of, and eventually all (PRIMER-1.0; Fig. 4d) of, the full EnKF QVAPOR uncertainty, the range of forecasted intensities increases. Also noticeable is an increase in the range of track forecasts with initial QVAPOR uncertainty (Figs. 4e,f). This is most likely tied to the β effect since the stronger members track farther to the north. This can be seen most easily in the PRIMER-1.0 (Fig. 4f) ensemble. To summarize, since QVAPOR within the pouch was the only variable that differed in the initial conditions of the PRIMER ensembles, we conclude that the uncertainty of initial moisture within the pouch region translates to noticeable uncertainty in the forecasted intensity.

The increase in intensity uncertainty with initial moisture uncertainty is associated with the propensity for the initially moister members to intensify earlier and reach a greater peak intensity. This is most noticeable for the PRIMER-1.0 (Fig. 4d) ensemble, where a clear stratification by initial QVAPOR is evident. We quantify this a bit further by showing the Pearson correlation coefficient between the initial QVAPOR and the intensity for each ensemble (Fig. 5a) forecast. Strong negative correlations exist between the initial QVAPOR and the minimum SLP in the PRIMER-1.0 ensemble. These correlations are statistically significant at greater than 95% confidence based on the Student's two-tailed t test (Gosset 1908) for almost all hours of the forecast (Fig. 5b). This supports our claim that initially moister members intensify earlier and more. As the initial QVAPOR uncertainty decreases, the correlation between the initial QVAPOR within the pouch and the minimum SLP becomes less negative (Fig. 5a) and less statistically significant (Fig. 5b). This trend is likely a result of the decreasing divergence between moist and dry members with decreasing initial moisture uncertainty. The correlation values are the most negative in the full EnKF ensemble forecast. This is because the members in the original analysis that have the lowest SLP tend to also have the most moisture in the pouch (not shown) because the PSU WRF-EnKF updates QVAPOR via the ensemble correlations that exist between it and other variables. Ultimately, ensemble members with more moisture within the initial pouch region will intensify earlier and reach a greater peak intensity, thus causing the intensity uncertainty to be greater when the initial moisture uncertainty is greater.

We conclude this subsection by showing the growth of intensity uncertainty (Fig. 6) in terms of ensemble spread of minimum SLP. The ensemble spread of minimum SLP grows for all moisture modification ensembles (Fig. 6a) up to about the point when intensification paused in the best track data (~40 h after the observed genesis time). After that point, the ensemble spread decreased, indicating the members generally agreed intensification would pause. Also evident in Fig. 6a is the trend toward greater intensity uncertainty as the initial

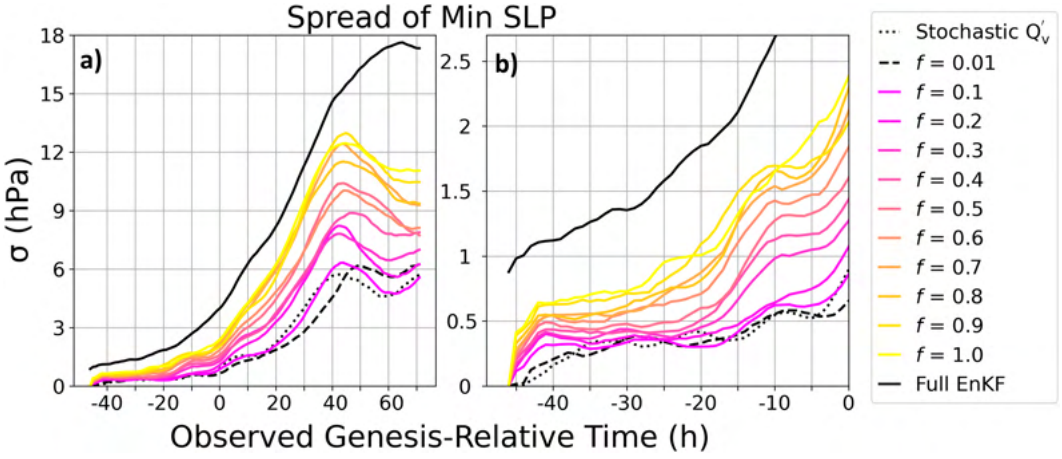

FIG. 6. (a) Ensemble spread of the minimum SLP (hPa) within 300 km of the storm center for each ensemble forecast. (b) The first 46 h of (a). Note the y axis is different in each subplot.

QVAPOR uncertainty within the pouch increased, consistent with Fig. 4. Note the spread of minimum SLP for the full EnKF ensemble begins at a nonzero value, maintains an almost constant vertical separation with the PRIMER-1.0 ensemble until about 40 h after the observed genesis time, and then continues to increase almost until the end of the forecast (Fig. 6a). This trend implies that the initial uncertainty in the non-QVAPOR values of the full EnKF ensemble might have played only a minor role in the intensity uncertainty until well after the observed genesis time. By comparing the PRIMER-1.0 ensemble spread of minimum SLP to that of the full EnKF ensemble in Fig. 6a, we conclude that initial moisture uncertainty within the incipient disturbance plays a crucial role in determining the intensity uncertainty during the hours leading up to the observed genesis time.

Intensity uncertainty evolution before the observed genesis time is shown more closely in Fig. 6b. Figure 6b reveals three phases in the evolution of intensity uncertainty during the hours leading up to the observed genesis time. The first phase sees a rapid growth of uncertainty during the first 6 h. After the period of rapid uncertainty growth, a roughly 12-h period of quasi-steady values followed. Beginning at about 30 h before the observed genesis time, the ensemble spread increases once again and continues through genesis time. At the start of the last phase, the ensembles with greater initial QVAPOR uncertainty already had larger intensity uncertainty, enabling them to achieve even larger uncertainties by the observed genesis time. This three-phase pattern will be discussed in the next two subsections.

b. *Impact of initial moisture uncertainty on the growth of convective differences*

This subsection investigates more closely the divergence of forecasts within each ensemble prior to genesis. To focus on the meso-β scale (i.e., 20–200 km), we calculate the volume-averaged difference kinetic energy (DKE) within a 2° × 2° box centered on the storm center. The DKE between any two ensemble members is given by

$$\mathrm{DKE}_{i,j,k} = \frac{1}{2}u'^2_{i,j,k} + \frac{1}{2}v'^2_{i,j,k}, \tag{1}$$

where $u'^2_{i,j,k}$ and $v'^2_{i,j,k}$ are the differences between the u and v wind components at each location in storm-relative coordinates. The DKE at each location is then averaged over the 1770 combinations $\binom{60}{2}$ of ensemble member pairs before taking a volume average. Figure 7 shows the trend of DKE during the hours leading up to the observed genesis time. It resembles the ensemble spread in minimum SLP (Fig. 6b); however, it is smoother and increases monotonically with initial moisture uncertainty. The rapid divergence of the ensemble forecasts during the first few hours appears quite prominent in the DKE plots. Close inspection reveals a local maximum of DKE occurs between 8 and 10 h after initialization (38–36 h before the observed genesis), which is about 4–6 h after the minimum SLP spread flattens out (see Fig. 6b). This subtle discrepancy might be a consequence of changes in wind speed lagging that of changes in minimum SLP. Another interesting trend in Fig. 7 is the decrease in DKE from about 38 to almost 30 h before the observed genesis time, which are times when the spread of minimum SLP remained quasi-steady. The dip in DKE during these times might reflect changes in the structure of the vortex as well as the potential impact of a diurnal cycle (discussed later). Since DKE (a bulk quantity) and ensemble spread of minimum SLP (a point metric) are two very different ways of quantifying the divergence of the intensity forecasts, it should not be surprising that they exhibit some differences. In summary, multiple metrics reveal a rapid divergence of the intensity forecasts during the first 6 h, followed by a roughly 12-h pause in divergence, before rapidly diverging through the observed genesis time.

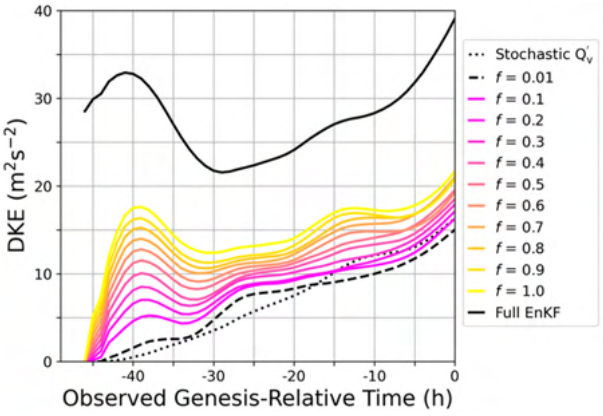

FIG. 7. Volume-averaged DKE ($m^2\ s^{-2}$) computed within a 2° × 2° box centered on the storm center for each ensemble forecast.

Upscale growth of errors to the pouch scale can be seen in convective differences. Figure 8 shows spaghetti plots of the 210-K simulated *Meteosat-10* channel 6 BT contour in the region where initial QVAPOR perturbations were modified. Channel 6, with a central wavelength of 7.3 μm (Schmid 2000), is sensitive to lower-tropospheric water vapor. Note that this channel was not assimilated in this study. The 210-K contour represents cold cloud tops, indicative of deep convection. After 1 h of integration, all 60 members in both PRIMER-0.01 (Fig. 8a_1) and PRIMER-0.1 (Fig. 8b_1) ensembles agree on the positioning of this contour (i.e., deep convection). At this time, a large MCS can be seen in the western half of the pouch region. When initial QVAPOR uncertainty is increased to half of the full EnKF, slight discrepancies in the positioning of this contour become noticeable within 1 h (Fig. 8c_1). These discrepancies, which show the small coverage differences in that MCS among members, are due to small differences in its intensity across members. These intensity differences become more noticeable when the initial QVAPOR uncertainty is increased to the full EnKF (Fig. 8d_1). Some members in PRIMER-1.0 develop new convection in the southern and eastern parts of the pouch region after 1 h. As it is integrated further, these members develop the new convection, while others subsequently develop their own new

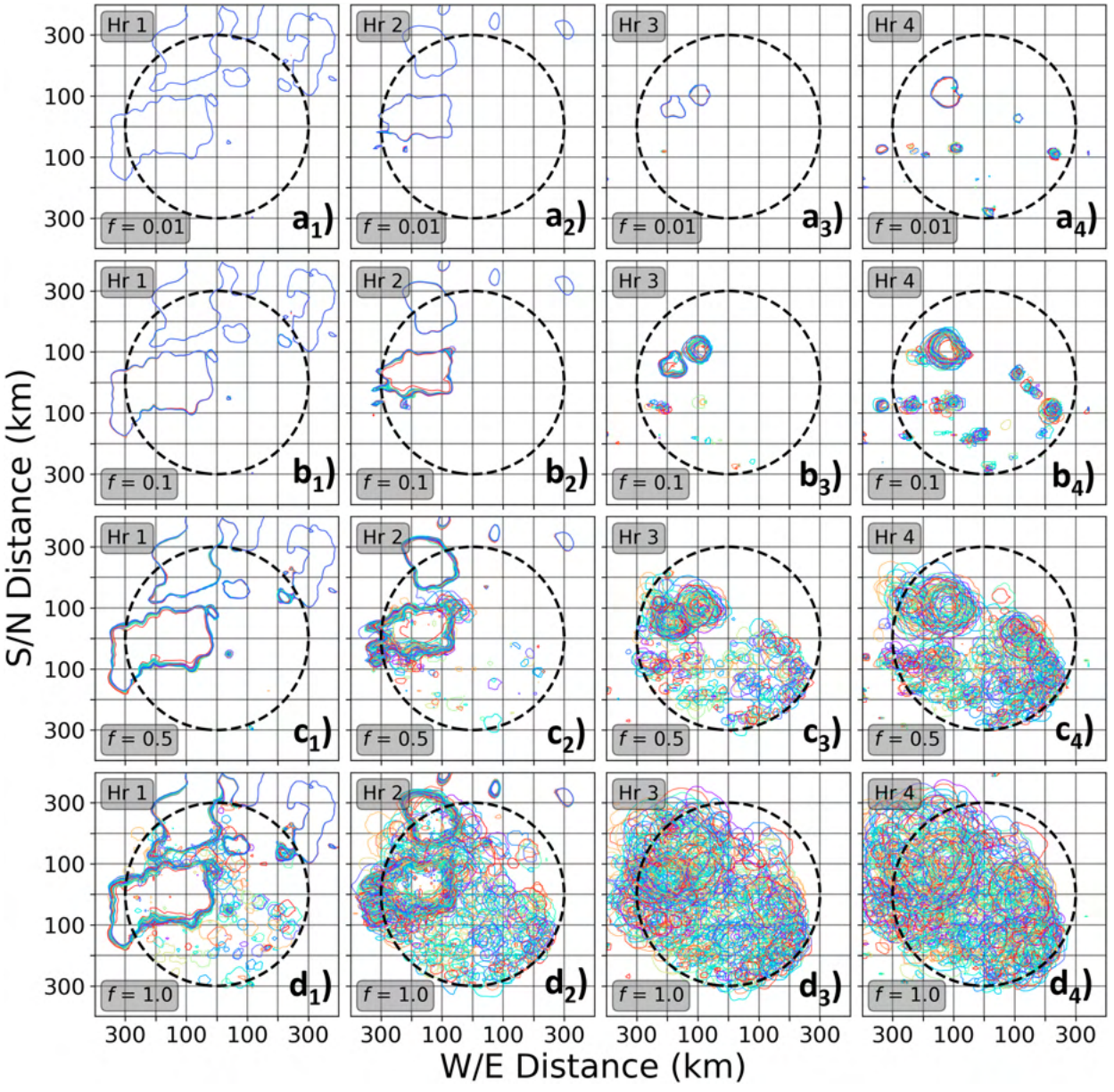

FIG. 8. Spaghetti plots of the 210-K *Meteosat-10* simulated channel 6 BT contour for the ensemble initialized with (a_1)–(a_4) PRIMER-0.01, (b_1)–(b_4) PRIMER-0.1, (c_1)–(c_4) PRIMER-0.5, and (d_1)–(d_4) PRIMER-1.0 moisture perturbations at lead times of (first column) 1, (second column) 2, (third column) 3, and (fourth column) 4 h. In each subplot, the origin is the initial sweet spot location, the black dashed circle demarcates the area in which the initial moisture perturbations were modified, and the color of each contour represents the initial moisture content of each member as in Fig. 3.

convection in other positions (Fig. 8d_2). By hours 3 (Fig. 8d_3) and 4 (Fig. 8d_4), through a combination of MCS dislocation and intensity errors, convective differences in the PRIMER-1.0 ensemble have spread throughout the entire region of the initial pouch. This process ensues for all ensemble forecasts; however, its onset appears later as initial QVAPOR uncertainty decreases. For example, the PRIMER-0.5 ensemble shows signs of dislocation errors cropping up after 2 h of integration (Fig. 8c_2), PRIMER-0.1 after 3–4 h (Figs. 8b_3,b_4) and PRIMER-0.01 after about 6 h (not shown). There appears to be no visible relationship between the initial QVAPOR of a particular member and either where new convection develops or how large the MCSs are. This shows how truly nonlinear and stochastic the system is. The take-home message of Fig. 8 is that greater initial moisture uncertainty within the pouch region leads to earlier development of dislocation errors in future MCSs, and these dislocation errors rapidly grow to overwhelm the area of the pouch.

Before discussing the impacts of initial moisture uncertainty on pathways to genesis and its timing, we summarize the key finding of this subsection: Increasing the uncertainty in the

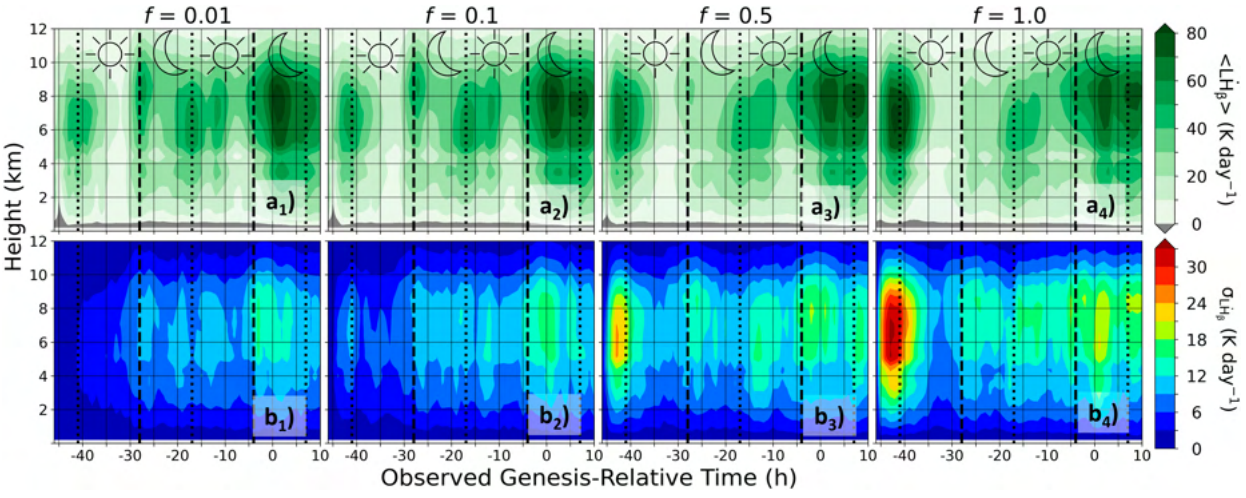

FIG. 9. Temporal evolution of the (a_1)–(a_4) ensemble mean and (b_1)–(b_4) ensemble spread of the meso-β-scale latent heating rates (K day^{-1}) for the ensemble initialized with (a_1),(b_1) PRIMER-0.01, (a_2),(b_2) PRIMER-0.1, (a_3),(b_3) PRIMER-0.5, and (a_4),(b_4) PRIMER-1.0 moisture perturbations. The meso-β-scale latent heating rate at each time was found by averaging the latent heating rates within a $2^\circ \times 2^\circ$ box centered on the storm center. In each subplot, dotted vertical lines indicate sunrise and dashed vertical lines represent sunset.

initial moisture content within 300 km of the pouch center leads to larger uncertainty in the intensity forecast during the first 6–12 h due to an earlier development and faster growth of MCS dislocation and intensity differences.

c. *Impact of initial moisture uncertainty on pathways to genesis and genesis timing*

In the previous subsection, we showed that rapid growth of convective differences to the scale of the pouch occurs due to initial moisture uncertainty within it. This subsection reveals the impacts of these errors on pathways to genesis and genesis timing.

The rapid development of pouch-scale convective differences associated with the initial QVAPOR uncertainty within it can be inferred from meso-β-scale latent heating rates (Fig. 9). In an ensemble mean sense (Figs. 9a_1–a_4), latent heating rates in each PRIMER forecast follow the same general evolution; however, uncertainty in their magnitude, as shown by the ensemble spread of meso-β-scale latent heating rates (Figs. 9b_1–b_4), increases with initial QVAPOR uncertainty. Although all PRIMER ensembles exhibit peaks in the spread of latent heating rates coincident with the timing of convective bursts shown in the ensemble mean, the PRIMER-1.0 ensemble has noticeably larger uncertainty in the strength of those bursts (Fig. 9b_4).

The timing of the convective bursts in the ensemble mean latent heating rates reveals a diurnal cycle, especially during the first day of integration. A prominent convective burst occurs during the first 6 h of all ensembles, peaking just before sunrise. After sunrise, convection in all ensembles is suppressed until about 30 h before observed genesis time—the approximate time of sunset. Recall the ensemble spread of intensity remained quasi-steady (Fig. 6b) and DKE dropped (Fig. 7) during the daylight hours between 42 and 30 h before the observed genesis time. During this period, the ensemble spread of meso-β-scale latent heating rates also remains quasi-steady or decreases slightly. At around 30 h before the observed genesis time, the sun begins to set, and another round of convective intensification starts. This new round of convection leads to an increase once again in the mean and spread of latent heating rates. Thus, the diurnal cycle of convection may have played a major role in the further growth of convective differences among members. The impact of the diurnal cycle on deep convection, as well as TC genesis and intensification, has been illustrated by numerous other studies (e.g., Hobgood 1986; Craig 1996; Ge et al. 2014; Melhauser and Zhang 2014; Tang and Zhang 2016; Bell and Montgomery 2019; Dunion et al. 2019; Ruppert et al. 2020; Wing 2022; Chen et al. 2023).

Another intriguing feature in the ensemble mean plots of meso-β-scale latent heating rates is the convective burst during the first 6 h of the forecast period, which increases in intensity with increasing initial QVAPOR uncertainty (Figs. 9a_1–a_4). This is a result of the model adjustment process in the first 6 h of integration. Since the PSU WRF-EnKF system provides a statistically based update to the state, some degree of physical imbalance is present in the analysis. Upon initialization, some of the convection present will dissipate as the model is integrated because the dynamics cannot support it. This dissipation process affects the initially moister ensemble members less than the drier ones. Since the ensembles that have the greatest initial QVAPOR uncertainty have more extremely moist members, the dissipation process will affect them less. This explains why the PRIMER-1.0 ensemble has the strongest convective burst during the first 6 h of the forecast. The physical imbalance described here is a common feature of DA systems (Houtekamer and Mitchell 2005; Poterjoy and Zhang 2014b) that cannot be avoided when starting from an analysis. How much of the rapid intensity spread growth during the first 6 h of integration (Fig. 6b)

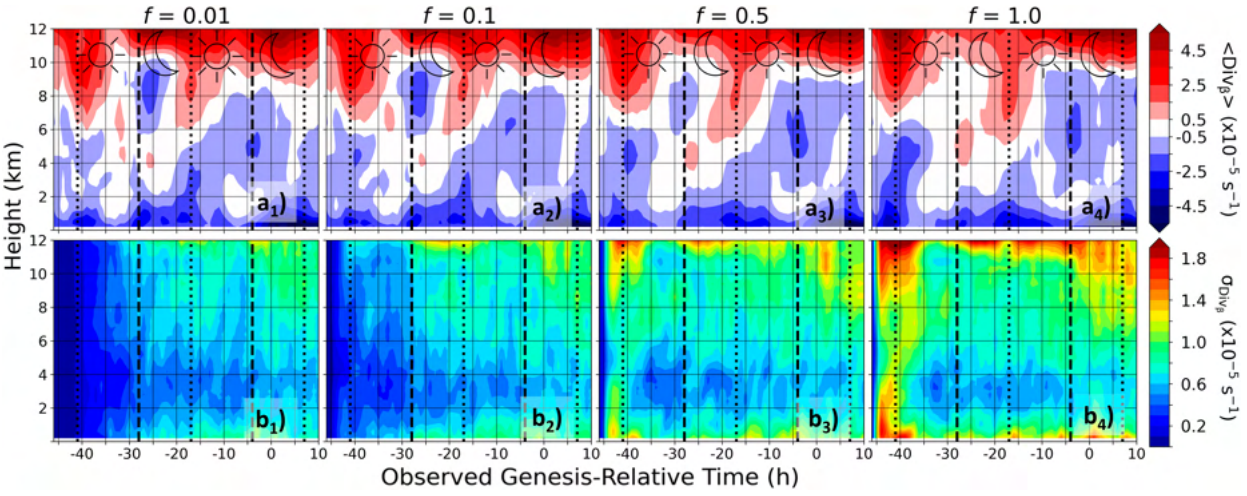

FIG. 10. As in Fig. 9, but for the meso-β-scale divergence ($\times 10^{-5}$ s^{-1}).

results from physical imbalance present at initialization is unclear; however, it suffices to say that operational models will experience this effect as well.

The bursts of deep convection shown in Fig. 9 are associated with periods of enhanced low-level convergence through a deep layer, whereas times of suppressed convection experience weaker and shallower low-level convergence (Figs. 10a$_1$–a$_4$). Consistent with Figs. 9a$_1$–a$_4$, the low-level convergence during the first 6 h is progressively deeper and stronger with increasing initial QVAPOR uncertainty. During the daylight hours between 42 and 30 h before the observed genesis time, the lull in deep convection is accompanied by shallower, weaker low-level convergence. When the sun begins to set around 30 h before the observed genesis time, the low-level convergence once again grows deeper and stronger with the new round of convection. As with the latent heating rates, all PRIMER ensembles agree on the general trend of the meso-β-scale divergence in an ensemble mean sense (Figs. 10a$_1$–a$_4$), but they disagree on the uncertainty of its strength. Based on the ensemble spread of meso-β-scale divergence (Figs. 10b$_1$–b$_4$), uncertainty in the strength of low-level convergence associated with convective bursts increases as initial QVAPOR uncertainty increases.

Convective bursts and their associated low-level convergence play a role in the spinup of the low-level meso-β-scale vortex (Fig. 11). As with low-level convergence and latent heating rates, all PRIMER ensembles agree on the general trend of the relative vorticity in an ensemble mean sense (Figs. 11a$_1$–a$_4$). More specifically, the low-level vortex begins to intensify and extend upward during the early and late morning hours of the first day (i.e., 42–35 h before the observed genesis time). Around the middle of that day, the vortex at all levels begins to spin down, with the pattern clearest at low levels. Shortly after sunset on the first day, the low-level vortex once again begins to spin up. This time, however, vorticity continues to increase with height and time through the daylight hours of the second day to eventually become a TC. By comparing Figs. 10a$_1$–a$_4$ to Figs. 11a$_1$–a$_4$, one can see those changes in the low-level vorticity lag changes in the low-

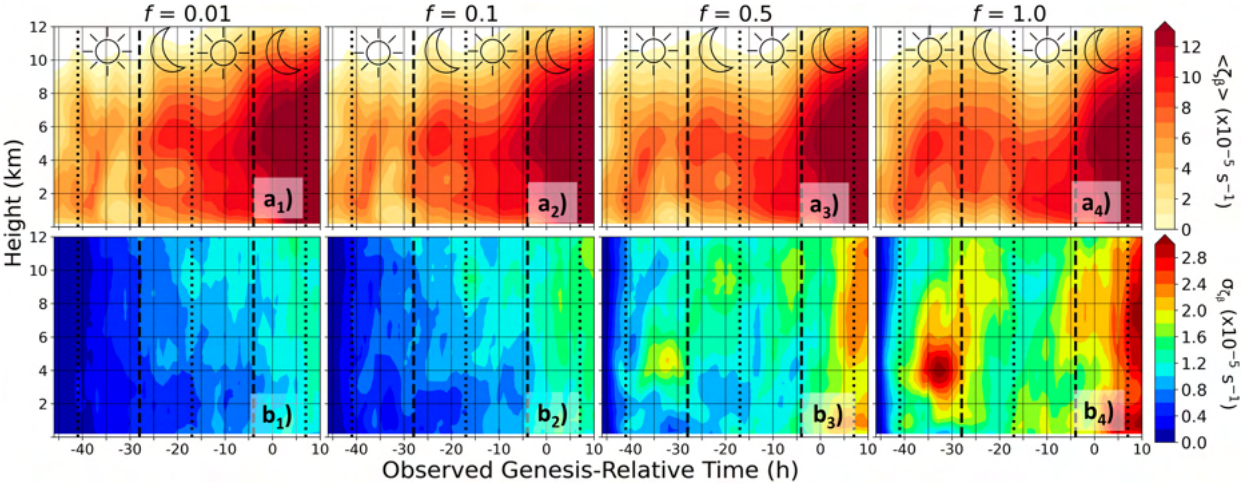

FIG. 11. As in Fig. 9, but for the meso-β-scale relative vorticity ($\times 10^{-5}$ s^{-1}).

level convergence. Consistent with Wang et al. (2010) and Bell and Montgomery (2019), this shows the role of the low-level meso-β-scale convergence associated with convective bursts in helping to spin up the vortex. An interesting pattern shown in Figs. 11a$_1$–a$_4$ is the temporary spindown of the low-level vortex during the afternoon and evening hours of the first day. This delayed genesis is influenced by the intense convective burst that occurred during the first 6 h combined with the subsequent lack of new convection during the daytime hours. Once that convection reaches maturity, evaporatively cooled downdrafts (not shown) reduce the meso-β-scale low-level convergence, thereby temporarily preventing further spinup of the low-level vortex. To summarize, convective bursts and their associated low-level convergence contribute to a spinup of the low-level vortex in an ensemble mean sense, regardless of the initial moisture uncertainty within the pouch.

Increasing uncertainty in the initial QVAPOR within the pouch leads to greater uncertainty in the strength of the meso-β-scale vortex at all levels (Figs. 11b$_1$–b$_4$). This uncertainty in the strength of the vortex grows rapidly during the early hours, especially for PRIMER-1.0 (Fig. 11b$_4$). For PRIMER-1.0, and to a lesser extent PRIMER-0.5 (Fig. 11b$_3$), large uncertainty in the strength of the midlevel vortex can be seen in the afternoon hours between 35 and 30 h before the observed genesis time. This lags the maximum in the ensemble mean midlevel vortex (Figs. 11a$_3$,a$_4$) by a few hours, indicating uncertainty in the timing of midlevel vortex spindown when initial QVAPOR uncertainty is greater. Conversely, both PRIMER-0.5 and PRIMER-1.0 display lower uncertainty in the spindown of the low-level vortex during those afternoon and evening hours. This is likely a result of the lack of new convection during these times. Once the sun sets around 30 h before the observed genesis time, new convection develops and the low-level vortex eventually spins up. The ensemble spread of the meso-β-scale relative vorticity subsequently increases in time from the surface upward (Figs. 11b$_1$–b$_4$). Ultimately, the timing of the spinup of the low-level vortex becomes more uncertain as the initial QVAPOR uncertainty within the pouch increases.

The differences in the timing of the spinup of the low-level vortex shown previously translate to differences in the timing of TC genesis among members. To corroborate that statement, we define the timing of genesis in the simulations. In this study, simulated genesis time will refer to the precise hour at which the 700–850-hPa layer-averaged meso-β-scale circulation exceeds a value of 8×10^{-5} s^{-1} and remains above that threshold for the remainder of the forecast period. This threshold value is chosen to be consistent with the study of Majumdar and Torn (2014). Based on the meso-β-scale circulation values plotted in Fig. 12, uncertainty in the simulated genesis time for this case study increases as the initial moisture uncertainty within the pouch region increases. More specifically, the ensemble spread of the simulated genesis time increases to over 6 h as the initial moisture uncertainty reaches that of the full EnKF analysis. The spread of simulated genesis time increases with increasing initial moisture uncertainty because the initially moistest members tend to undergo genesis earlier, as indicated by the correlation between initial moisture content and genesis time. Note that, consistent with Fig. 5, these correlations become increasingly negative and statistically significant as initial moisture uncertainty within the pouch increases. Finally, it is important to note that these findings are not sensitive to the choice of critical circulation threshold used.

Uncertainty in the simulated timing of TC genesis due to initial QVAPOR uncertainty within the pouch is a result of uncertainty in the strength and coverage of convective activity on the meso-β scale. This can be inferred from Fig. 13, which shows the statistically significant correlations between the initial QVAPOR within the pouch and the meso-β-scale averages of latent heating, divergence, and relative vorticity. Based on Fig. 13, initially moister members tend to produce greater rates of latent heat release (Fig. 13a), a stronger and deeper layer of low-level convergence (Fig. 13b), and a stronger low-level vortex (Fig. 13c) during the early hours of the forecast. After sunrise on the first day (~40–35 h before the observed genesis time), moister members tend to produce evaporative cooling below 4 km as the intense convection they produced has matured by this point. This evaporative cooling coincides with low-level divergence at that time for the initially moist members. Also at that time, the moister members tend to have stronger convergence near 4 km, which is consistent with the top-heavy latent heating profile (Figs. 9a$_1$–a$_4$) and is related to the prevalence of stratiform precipitation. Shortly thereafter (35–30 h before the observed genesis time), the moister members tend to have a stronger midlevel vortex near 4 km and a greater spindown (although not statistically significant) of the low-level vortex. As the sun sets that day, the moister members once again begin to release more latent heat at all levels, coincident with a new period of low-level convergence. By the end of the first full night (~20 h before the observed genesis time), the moister members have begun to spin up the low-level vortex after a prolonged period (~10 h) of enhanced low-level convergence. Ultimately, members that are initially moister tend to form a TC earlier because the intense convection they produce leads to the earlier spinup of a low-level vortex.

In this subsection, we have shown that, in the context of Hurricane Irma (2017), increasing the uncertainty in the initial moisture content within 300 km of the pouch center does not alter the pathway to TC genesis; however, it increases the uncertainty in genesis timing since ensemble members with more moisture exhibit an earlier spinup of the low-level vortex.

4. Discussion and conclusions

In this study, we investigated the impacts of local initial moisture uncertainty within the incipient disturbance that would become Hurricane Irma (2017) on the practical predictability of its formation and subsequent intensification. By comparing an ensemble forecast with only QVAPOR perturbations within the pouch region to one that retained perturbations of all variables domainwide, we found that initial moisture uncertainty within the incipient disturbance plays a crucial role in determining the predictability of TC genesis.

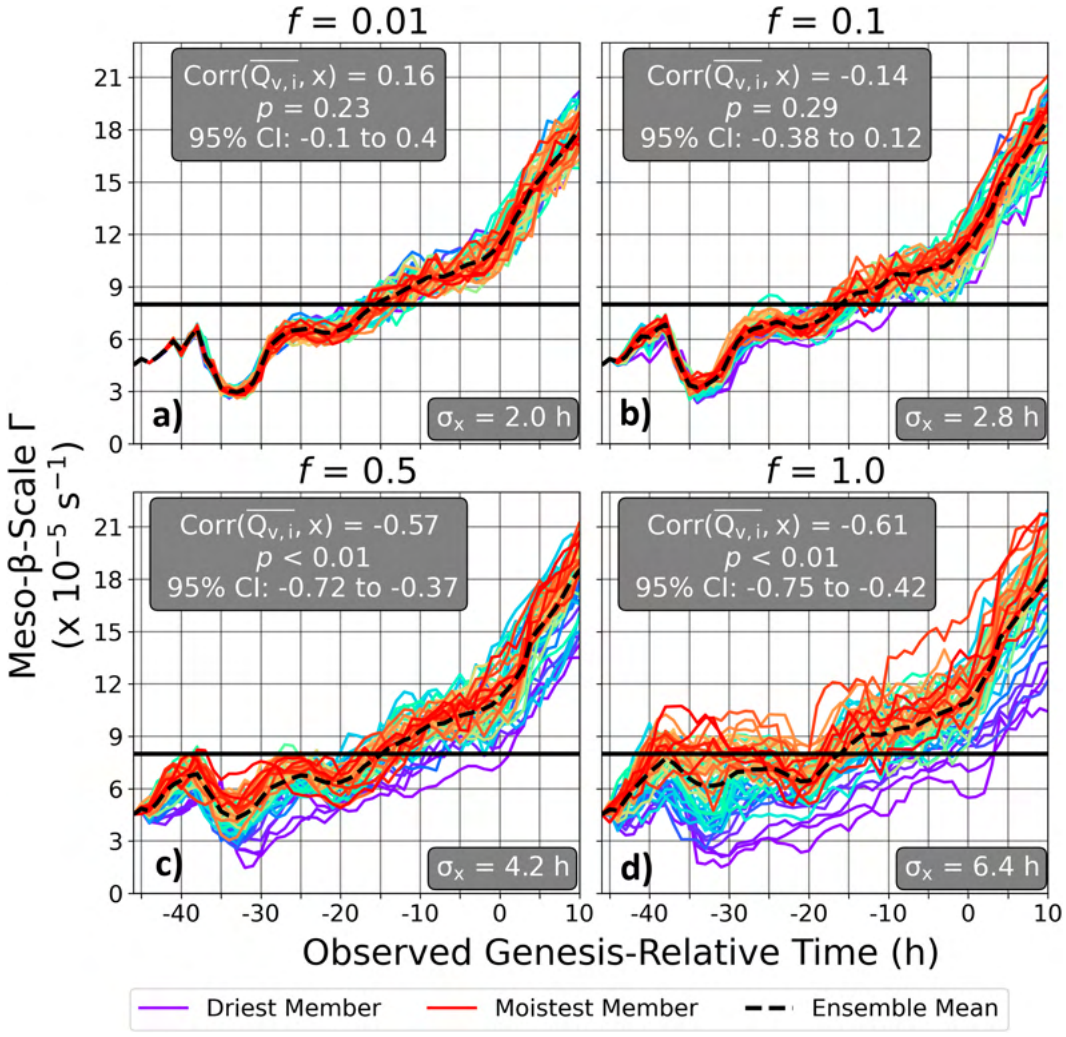

FIG. 12. Temporal evolution of the meso-β-scale circulation ($\times 10^{-5}$ s^{-1}) averaged within the 700–850-hPa layer for the ensemble initialized with (a) PRIMER-0.01, (b) PRIMER-0.1, (c) PRIMER-0.5, and (d) PRIMER-1.0 moisture perturbations. The meso-β-scale circulation at each time was found by averaging the relative vorticity within a 2° × 2° box centered on the storm center. Line colors represent the initial moisture content of each member as in Fig. 3. The circulation threshold of 8×10^{-5} s^{-1} used to identify genesis time in the simulations is demarcated by the solid horizontal black line. Listed in the lower right corner of each subplot is the ensemble spread of simulated genesis time (h). Finally, the upper-left corner of each subplot lists the Pearson correlation coefficient (with corresponding p value and 95% confidence interval) between the volume-averaged QVAPOR within 300 km of the initial sweet spot location and simulated genesis time.

Upon integration, initial moisture uncertainty causes the rapid growth of MCS intensity and dislocation errors that overwhelm the pouch region within a couple of hours. Eventually, pouch-scale differences in convection lead to a variety of genesis timings, with initially moister members spinning up a low-level vortex earlier. As initial moisture uncertainty is reduced by shrinking perturbations to QVAPOR, pouch-scale convective differences are slower to grow, and genesis timing is constrained.

This study suggests the practical predictability of TC genesis may be improved by reducing initial moisture uncertainty within the incipient disturbance of potential TCs. Consequently, it provides motivation to target this small, but critical, region, for high-resolution observations that modern DA systems can use to constrain the initial moisture within it. All-sky IR and MW observations, such as in this study, are one type of observation that can reduce moisture uncertainty. Beyond that, high-resolution in situ moisture observations at all levels within the disturbance will likely be needed (e.g., from a dense dropsonde network). Before such an investment, future studies should confirm the robustness of these results with other storms, given the strong case-to-case variability in genesis predictability associated with various flow regimes (Sippel et al. 2011; Melhauser and Zhang 2012; Torn and Cook 2013; Komaromi and Majumdar 2015). Future studies should also confirm the robustness of these results with higher-resolution models that

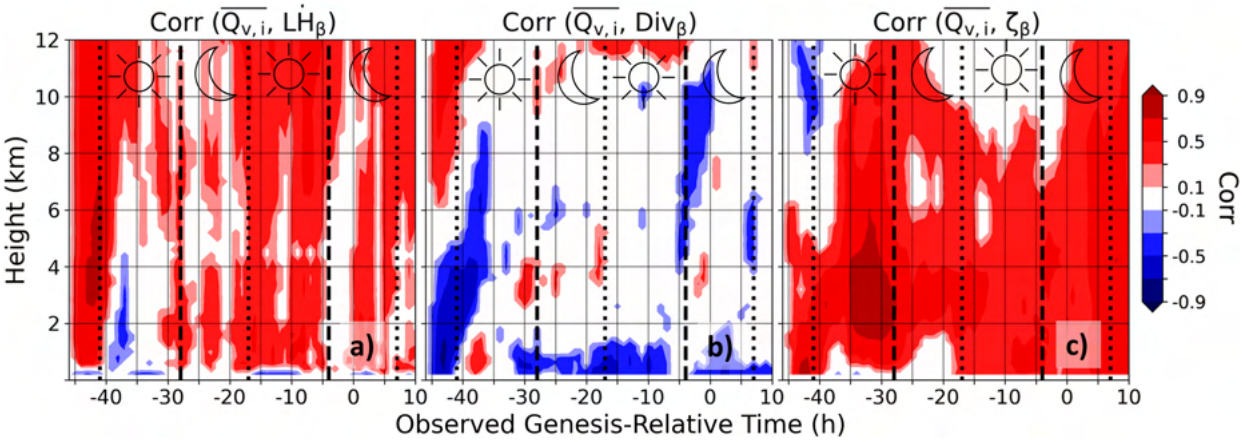

FIG. 13. Temporal evolution of the Pearson correlation coefficient between the initial-hour volume-averaged QVAPOR within 300 km of the pouch center and the meso-β-scale (a) latent heating rates, (b) divergence, and (c) relative vorticity for the ensemble initialized with PRIMER-1.0 moisture perturbations. Only correlations that are statistically significant at greater than 95% based on the Student's t test (Gosset 1908) are plotted. The meso-β-scale averages at each time were found by averaging within a 2° × 2° box centered on the storm center. In each subplot, dotted vertical lines indicate sunrise and dashed vertical lines represent sunset.

better resolve convective scale motions—both Zhang et al. (2003) and Zhang et al. (2007) revealed that the initial growth of errors becomes faster as resolution is increased. Another limitation of this study is that it neglects the potential impacts of initial moisture uncertainty within the environment. Finally, the spindown of the model during the first 6 h of integration and using a single forecast model and DA system are just some of the other limitations. Nevertheless, this study reveals a glimmer of hope. Not only does it show the improvement that can be brought to TC genesis forecasts by constraining moisture within a small region, but it also suggests tropical cyclogenesis might be more predictable than it seems. The latter point can be realized by noting perturbations to initial moisture well below the amplitude of any observation system at one model level in a small region lead to forecast uncertainty well below that of forecasts initialized from typical analysis uncertainty in all variables domain-wide (Fig. 6a).

Our results lead to some very interesting questions that are worth pursuing in the future. For example, how does the impact of initial moisture uncertainty within the pouch region compare to that of initial moisture uncertainty within the environment? Also, does constraining the initial moisture at certain vertical levels within the pouch impact the predictability of TC genesis more than others? Another factor worth considering is the influence of the diurnal cycle of convection on the predictability of TC genesis. During our analysis, we revealed the delayed genesis that occurred in the daylight hours on the first day. How might our results differ if the forecasts were initialized during different parts of the diurnal cycle? These are some of the questions we plan to pursue in the future.

Acknowledgments. This study is supported by the National Aeronautics and Space Administration (NASA) Grant 80NSSC22K0613, the Office of Naval Research (ONR) Grant N00014-18-1-2517, and the Office of Science of the U.S. Department of Energy Biological and Environmental Research as part of the Regional and Global Model Analysis program area. Computing was conducted at the Texas Advanced Computing Center (TACC). We would like to express our extreme gratitude to the editor, Dr. Jason Sippel, for overseeing the review of our manuscript, as well as Dr. Sharanya J. Majumdar and the two anonymous reviewers for their helpful comments. The comments have helped us to strengthen the science of our study and improve the quality and clarity of the manuscript. We are also thankful for the valuable suggestions and advice that came from fruitful discussions with Man-Yau Chan, Chris Davis, Richard Rotunno, and Zhu Yao.

Data availability statement. Initial conditions for all ensemble forecasts presented in this study can be freely downloaded from the Penn State Data Commons (https://doi.org/10.26208/15Q9-MM49). All assimilated GTS observations were obtained from datasets 351.0 and 461.0 of the NCAR Research Data Archive (https://rda.ucar.edu). All assimilated *Meteosat-10* SEVIRI channel 5 BTs were ordered from the EUMETSAT Data Centre (https://www.eumetsat.int/eumetsat-data-centre). All assimilated MW BTs were downloaded from the NASA GPM's Precipitation Processing System (https://storm.pps.eosdis.nasa.gov/storm/).

REFERENCES

Asaadi, A., G. Brunet, and M. K. Yau, 2016: On the dynamics of the formation of the Kelvin cat's-eye in tropical cyclogenesis. Part II: Numerical simulation. *J. Atmos. Sci.*, **73**, 2339–2359, https://doi.org/10.1175/JAS-D-15-0237.1.

——, ——, and ——, 2017: The importance of critical layer in differentiating developing from nondeveloping easterly waves. *J. Atmos. Sci.*, **74**, 409–417, https://doi.org/10.1175/JAS-D-16-0085.1.

Barker, D. M., W. Huang, Y.-R. Guo, A. J. Bourgeois, and Q. N. Xiao, 2004: A three-dimensional variational data assimilation system for MM5: Implementation and initial results. *Mon.*

Wea. Rev., **132**, 897–914, https://doi.org/10.1175/1520-0493(2004)132<0897:ATVDAS>2.0.CO;2.

Bell, M. M., and M. T. Montgomery, 2019: Mesoscale processes during the genesis of Hurricane Karl (2010). *J. Atmos. Sci.*, **76**, 2235–2255, https://doi.org/10.1175/JAS-D-18-0161.1.

Berry, G. J., and C. D. Thorncroft, 2012: African easterly wave dynamics in a mesoscale numerical model: The upscale role of convection. *J. Atmos. Sci.*, **69**, 1267–1283, https://doi.org/10.1175/JAS-D-11-099.1.

Brammer, A., and C. D. Thorncroft, 2015: Variability and evolution of African easterly wave structures and their relationship with tropical cyclogenesis over the eastern Atlantic. *Mon. Wea. Rev.*, **143**, 4975–4995, https://doi.org/10.1175/MWR-D-15-0106.1.

——, ——, and J. P. Dunion, 2018: Observations and predictability of a nondeveloping tropical disturbance over the eastern Atlantic. *Mon. Wea. Rev.*, **146**, 3079–3096, https://doi.org/10.1175/MWR-D-18-0065.1.

Braun, S. A., and Coauthors, 2013: NASA's Genesis and Rapid Intensification Processes (GRIP) field experiment. *Bull. Amer. Meteor. Soc.*, **94**, 345–363, https://doi.org/10.1175/BAMS-D-11-00232.1.

Cangialosi, J. P., A. S. Latto, and R. Berg, 2018: Tropical cyclone report: Hurricane Irma (AL112017), 30 August–12 September 2017. NHC Tech. Rep., 111 pp., https://www.nhc.noaa.gov/data/tcr/AL112017_Irma.pdf.

Chan, M.-Y., and X. Chen, 2022: Improving the analyses and forecasts of a tropical squall line using upper tropospheric infrared satellite observations. *Adv. Atmos. Sci.*, **39**, 733–746, https://doi.org/10.1007/s00376-021-0449-8.

——, F. Zhang, X. Chen, and L. R. Leung, 2020: Potential impacts of assimilating all-sky satellite infrared radiances on convection-permitting analysis and prediction of tropical convection. *Mon. Wea. Rev.*, **148**, 3203–3224, https://doi.org/10.1175/MWR-D-19-0343.1.

Chen, X., and F. Zhang, 2019a: Development of a convection-permitting air-sea-coupled ensemble data assimilation system for tropical cyclone prediction. *J. Adv. Model. Earth Syst.*, **11**, 3474–3496, https://doi.org/10.1029/2019MS001795.

——, and ——, 2019b: Relative roles of preconditioning moistening and global circumnavigating mode on the MJO convective initiation during DYNAMO. *Geophys. Res. Lett.*, **46**, 1079–1087, https://doi.org/10.1029/2018GL080987.

——, O. M. Pauluis, L. R. Leung, and F. Zhang, 2018a: Multiscale atmospheric overturning of the Indian summer monsoon as seen through isentropic analysis. *J. Atmos. Sci.*, **75**, 3011–3030, https://doi.org/10.1175/JAS-D-18-0068.1.

——, ——, and F. Zhang, 2018b: Atmospheric overturning across multiple scales of an MJO event during the CINDY/DYNAMO campaign. *J. Atmos. Sci.*, **75**, 381–399, https://doi.org/10.1175/JAS-D-17-0060.1.

——, L. R. Leung, Z. Feng, F. Song, and Q. Yang, 2021: Mesoscale convective systems dominate the energetics of the South Asian summer monsoon onset. *Geophys. Res. Lett.*, **48**, e2021GL094873, https://doi.org/10.1029/2021GL094873.

——, ——, ——, and ——, 2022a: Crucial role of mesoscale convective systems in the vertical mass, water, and energy transports of the South Asian summer monsoon. *J. Climate*, **35**, 91–108, https://doi.org/10.1175/JCLI-D-21-0124.1.

——, ——, ——, and Q. Yang, 2022b: Precipitation-moisture coupling over tropical oceans: Sequential roles of shallow, deep, and mesoscale convective systems. *Geophys. Res. Lett.*, **49**, e2022GL097836, https://doi.org/10.1029/2022GL097836.

——, ——, ——, and ——, 2023: Diurnal MCSs precede the genesis of Tropical Cyclone Mora (2017): The role of convectively forced gravity waves. *J. Atmos. Sci.*, **80**, 1463–1479, https://doi.org/10.1175/JAS-D-22-0203.1.

Craig, G. C., 1996: Numerical experiments on radiation and tropical cyclones. *Quart. J. Roy. Meteor. Soc.*, **122**, 415–422, https://doi.org/10.1002/qj.49712253006.

Doyle, J. D., C. A. Reynolds, C. Amerault, and J. Moskaitis, 2012: Adjoint sensitivity and predictability of tropical cyclogenesis. *J. Atmos. Sci.*, **69**, 3535–3557, https://doi.org/10.1175/JAS-D-12-0110.1.

Dunion, J. P., C. D. Thorncroft, and D. S. Nolan, 2019: Tropical cyclone diurnal cycle signals in a hurricane nature run. *Mon. Wea. Rev.*, **147**, 363–388, https://doi.org/10.1175/MWR-D-18-0130.1.

Dunkerton, T. J., M. T. Montgomery, and Z. Wang, 2009: Tropical cyclogenesis in a tropical wave critical layer: Easterly waves. *Atmos. Chem. Phys.*, **9**, 5587–5646, https://doi.org/10.5194/acp-9-5587-2009.

Emanuel, K., 2018: 100 years of progress in tropical cyclone research. *A Century of Progress in Atmospheric and Related Sciences: Celebrating the American Meteorological Society Centennial*, *Meteor. Monogr.*, No 59, Amer. Meteor. Soc., https://doi.org/10.1175/AMSMONOGRAPHS-D-18-0016.1.

Gaspari, G., and S. E. Cohn, 1999: Construction of correlation functions in two and three dimensions. *Quart. J. Roy. Meteor. Soc.*, **125**, 723–757, https://doi.org/10.1002/qj.49712555417.

Ge, X., Y. Ma, S. Zhou, and T. Li, 2014: Impacts of the diurnal cycle of radiation on tropical cyclone intensification and structure. *Adv. Atmos. Sci.*, **31**, 1377–1385, https://doi.org/10.1007/s00376-014-4060-0.

Gosset, W. S., 1908: The probable error of a mean. *Biometrika*, **6** (1), 1–25, https://doi.org/10.2307/2331554.

Green, B. W., and F. Zhang, 2013: Impacts of air–sea flux parameterizations on the intensity and structure of tropical cyclones. *Mon. Wea. Rev.*, **141**, 2308–2324, https://doi.org/10.1175/MWR-D-12-00274.1.

Hall, N. M. J., G. N. Kiladis, and C. D. Thorncroft, 2006: Three-dimensional structure and dynamics of African easterly waves. Part II: Dynamical modes. *J. Atmos. Sci.*, **63**, 2231–2245, https://doi.org/10.1175/JAS3742.1.

Halperin, D. J., H. E. Fuelberg, R. E. Hart, J. H. Cossuth, P. Sura, and R. J. Pasch, 2013: An evaluation of tropical cyclone genesis forecasts from global numerical models. *Wea. Forecasting*, **28**, 1423–1445, https://doi.org/10.1175/WAF-D-13-00008.1.

Han, Y., P. van Delst, Q. Liu, F. Weng, B. Yan, R. Treadon, and J. Derber, 2006: JCSDA Community Radiative Transfer Model (CRTM): version 1. NOAA Tech. Rep. NESDIS-122, 31 pp., https://repository.library.noaa.gov/view/noaa/1157.

——, F. Weng, Q. Liu, and P. van Delst, 2007: A fast radiative transfer model for SSMIS upper atmosphere sounding channels. *J. Geophys. Res.*, **112**, D11121, https://doi.org/10.1029/2006JD008208.

Hartman, C. M., X. Chen, and M.-Y. Chan, 2023: Improving tropical cyclogenesis forecasts of Hurricane Irma (2017) through the assimilation of all-sky infrared brightness temperatures. *Mon. Wea. Rev.*, **151**, 837–853, https://doi.org/10.1175/MWR-D-22-0196.1.

He, J., and Coauthors, 2019: Development and evaluation of an ensemble-based data assimilation system for regional reanalysis over the Tibetan Plateau and surrounding regions. *J. Adv.*

Model. Earth Syst., **11**, 2503–2522, https://doi.org/10.1029/2019MS001665.

Hendricks, E. A., M. T. Montgomery, and C. A. Davis, 2004: The role of "vortical" hot towers in the formation of tropical cyclone Diana (1984). *J. Atmos. Sci.*, **61**, 1209–1232, https://doi.org/10.1175/1520-0469(2004)061<1209:TROVHT>2.0.CO;2.

Hobgood, J. S., 1986: A possible mechanism for the diurnal oscillations of tropical cyclones. *J. Atmos. Sci.*, **43**, 2901–2922, https://doi.org/10.1175/1520-0469(1986)043<2901:APMFTD>2.0.CO;2.

Hong, S.-Y., Y. Noh, and J. Dudhia, 2006: A new vertical diffusion package with an explicit treatment of entrainment processes. *Mon. Wea. Rev.*, **134**, 2318–2341, https://doi.org/10.1175/MWR3199.1.

Hopsch, S. B., C. D. Thorncroft, and K. R. Tyle, 2010: Analysis of African easterly wave structures and their role in influencing tropical cyclogenesis. *Mon. Wea. Rev.*, **138**, 1399–1419, https://doi.org/10.1175/2009MWR2760.1.

Hou, A. Y., and Coauthors, 2014: The Global Precipitation Measurement mission. *Bull. Amer. Meteor. Soc.*, **95**, 701–722, https://doi.org/10.1175/BAMS-D-13-00164.1.

Houtekamer, P. L., and H. L. Mitchell, 2005: Ensemble Kalman filtering. *Quart. J. Roy. Meteor. Soc.*, **131**, 3269–3289, https://doi.org/10.1256/qj.05.135.

Iacono, M. J., J. S. Delamere, E. J. Mlawer, M. W. Shephard, S. A. Clough, and W. D. Collins, 2008: Radiative forcing by long-lived greenhouse gases: Calculations with the AER radiative transfer models. *J. Geophys. Res.*, **113**, D13103, https://doi.org/10.1029/2008JD009944.

Komaromi, W. A., 2013: An investigation of composite dropsonde profiles for developing and nondeveloping tropical waves during the 2010 PREDICT field campaign. *J. Atmos. Sci.*, **70**, 542–558, https://doi.org/10.1175/JAS-D-12-052.1.

——, and S. J. Majumdar, 2015: Ensemble-based error and predictability metrics associated with tropical cyclogenesis. Part II: Wave-relative framework. *Mon. Wea. Rev.*, **143**, 1665–1686, https://doi.org/10.1175/MWR-D-14-00286.1.

Lawton, Q. A., and S. J. Majumdar, 2023: Convectively coupled Kelvin waves and tropical cyclogenesis: Connections through convection and moisture. *Mon. Wea. Rev.*, **151**, 1647–1666, https://doi.org/10.1175/MWR-D-23-0005.1.

——, ——, K. Dotterer, C. Thorncroft, and C. J. Schreck III, 2022: The influence of convectively coupled Kelvin waves on African easterly waves in a wave-following framework. *Mon. Wea. Rev.*, **150**, 2055–2072, https://doi.org/10.1175/MWR-D-21-0321.1.

Leppert, K. D., II, D. J. Cecil, and W. A. Petersen, 2013a: Relation between tropical easterly waves, convection, and tropical cyclogenesis: A Lagrangian perspective. *Mon. Wea. Rev.*, **141**, 2649–2668, https://doi.org/10.1175/MWR-D-12-00217.1.

——, W. A. Petersen, and D. J. Cecil, 2013b: Electrically active convection in tropical easterly waves and implications for tropical cyclogenesis in the Atlantic and East Pacific. *Mon. Wea. Rev.*, **141**, 542–556, https://doi.org/10.1175/MWR-D-12-00174.1.

Li, Z., and Z. Pu, 2014: Numerical simulations of the genesis of Typhoon Nuri (2008): Sensitivity to initial conditions and implications for the roles of intense convection and moisture conditions. *Wea. Forecasting*, **29**, 1402–1424, https://doi.org/10.1175/WAF-D-14-00003.1.

Majumdar, S. J., and R. D. Torn, 2014: Probabilistic verification of global and mesoscale ensemble forecasts of tropical cyclogenesis. *Wea. Forecasting*, **29**, 1181–1198, https://doi.org/10.1175/WAF-D-14-00028.1.

Melhauser, C., and F. Zhang, 2012: Practical and intrinsic predictability of severe and convective weather at the mesoscales. *J. Atmos. Sci.*, **69**, 3350–3371, https://doi.org/10.1175/JAS-D-11-0315.1.

——, and ——, 2014: Diurnal radiation cycle impact on the pregenesis environment of Hurricane Karl (2010). *J. Atmos. Sci.*, **71**, 1241–1259, https://doi.org/10.1175/JAS-D-13-0116.1.

Minamide, M., and F. Zhang, 2017: Adaptive observation error inflation for assimilating all-sky satellite radiance. *Mon. Wea. Rev.*, **145**, 1063–1081, https://doi.org/10.1175/MWR-D-16-0257.1.

Montgomery, M. T., M. E. Nicholls, T. A. Cram, and A. B. Saunders, 2006: A vortical hot tower route to tropical cyclogenesis. *J. Atmos. Sci.*, **63**, 355–386, https://doi.org/10.1175/JAS3604.1.

——, L. L. Lussier III, R. W. Moore, and Z. Wang, 2010a: The genesis of Typhoon Nuri as observed during the Tropical Cyclone Structure 2008 (TCS-08) field experiment—Part 1: The role of the easterly wave critical layer. *Atmos. Chem. Phys.*, **10**, 9879–9900, https://doi.org/10.5194/acp-10-9879-2010.

——, Z. Wang, and T. J. Dunkerton, 2010b: Coarse, intermediate and high resolution numerical simulations of the transition of a tropical wave critical layer to a tropical storm. *Atmos. Chem. Phys.*, **10**, 10 803–10 827, https://doi.org/10.5194/acp-10-10803-2010.

——, and Coauthors, 2012: The Pre-Depression Investigation of Cloud-Systems in the Tropics (PREDICT) experiment: Scientific basis, new analysis tools, and some first results. *Bull. Amer. Meteor. Soc.*, **93**, 153–172, https://doi.org/10.1175/BAMS-D-11-00046.1.

Núñez Ocasio, K. M., 2021: Tropical cyclogenesis and its relation to interactions between African easterly waves and mesoscale convective systems. Ph.D. dissertation, The Pennsylvania State University, 123 pp., https://etda.libraries.psu.edu/catalog/21775kmn18.

——, J. L. Evans, and G. S. Young, 2020: A wave-relative framework analysis of AEW–MCS interactions leading to tropical cyclogenesis. *Mon. Wea. Rev.*, **148**, 4657–4671, https://doi.org/10.1175/MWR-D-20-0152.1.

——, A. Brammer, J. L. Evans, G. S. Young, and Z. L. Moon, 2021: Favorable monsoon environment over eastern Africa for subsequent tropical cyclogenesis of African easterly waves. *J. Atmos. Sci.*, **78**, 2911–2925, https://doi.org/10.1175/JAS-D-20-0339.1.

Ou, T., D. Chen, X. Chen, C. Lin, K. Yang, H.-W. Lai, and F. Zhang, 2020: Simulation of summer precipitation diurnal cycles over the Tibetan Plateau at the gray-zone grid spacing for cumulus parameterization. *Climate Dyn.*, **54**, 3525–3539, https://doi.org/10.1007/s00382-020-05181-x.

Peng, M. S., B. Fu, T. Li, and D. E. Stevens, 2012: Developing versus nondeveloping disturbances for tropical cyclone formation. Part I: North Atlantic. *Mon. Wea. Rev.*, **140**, 1047–1066, https://doi.org/10.1175/2011MWR3617.1.

Poterjoy, J., and F. Zhang, 2014a: Predictability and genesis of Hurricane Karl (2010) examined through the EnKF assimilation of field observations collected during PREDICT. *J. Atmos. Sci.*, **71**, 1260–1275, https://doi.org/10.1175/JAS-D-13-0291.1.

——, and ——, 2014b: Intercomparison and coupling of ensemble and four-dimensional variational data assimilation methods for the analysis and forecasting of Hurricane Karl (2010). *Mon.*

Wea. Rev., **142**, 3347–3364, https://doi.org/10.1175/MWR-D-13-00394.1.

Rajasree, V. P. M., A. P. Kesarkar, J. N. Bhate, V. Singh, U. Umakanth, and T. H. Varma, 2016a: A comparative study on the genesis of north Indian Ocean tropical cyclone Madi (2013) and Atlantic Ocean tropical cyclone Florence (2006). *J. Geophys. Res. Atmos.*, **121**, 13 826–13 858, https://doi.org/10.1002/2016JD025412.

——, ——, ——, U. Umakanth, V. Singh, and T. Harish Varma, 2016b: Appraisal of recent theories to understand cyclogenesis pathways of tropical cyclone Madi (2013). *J. Geophys. Res. Atmos.*, **121**, 8949–8982, https://doi.org/10.1002/2016JD025188.

Ruppert, J. H., Jr., A. A. Wing, X. Tang, and E. L. Duran, 2020: The critical role of cloud–infrared radiation feedback in tropical cyclone development. *Proc. Natl. Acad. Sci. USA*, **117**, 27 884–27 892, https://doi.org/10.1073/pnas.2013584117.

Russell, J. O. H., and A. Aiyyer, 2020: The potential vorticity structure and dynamics of African easterly waves. *J. Atmos. Sci.*, **77**, 871–890, https://doi.org/10.1175/JAS-D-19-0019.1.

——, ——, and J. Dylan White, 2020: African easterly wave dynamics in convection-permitting simulations: Rotational stratiform instability as a conceptual model. *J. Adv. Model. Earth Syst.*, **12**, e2019MS001706, https://doi.org/10.1029/2019MS001706.

Schmid, J., 2000: The SEVIRI instrument. *Proc. 2000 EUMETSAT Meteorological Satellite Data User's Conf.*, Bologna, Italy, EUMETSAT, 13–32, https://www-cdn.eumetsat.int/files/2020-04/pdf_ten_msg_seviri_instrument.pdf.

Schreck, C. J., III, 2015: Kelvin waves and tropical cyclogenesis: A global survey. *Mon. Wea. Rev.*, **143**, 3996–4011, https://doi.org/10.1175/MWR-D-15-0111.1.

——, 2016: Convectively coupled Kelvin waves and tropical cyclogenesis in a semi-Lagrangian framework. *Mon. Wea. Rev.*, **144**, 4131–4139, https://doi.org/10.1175/MWR-D-16-0237.1.

Sieron, S. B., E. E. Clothiaux, F. Zhang, Y. Lu, and J. A. Otkin, 2017: Comparison of using distribution-specific versus effective radius methods for hydrometeor single-scattering properties for all-sky microwave satellite radiance simulations with different microphysics parameterization schemes. *J. Geophys. Res. Atmos.*, **122**, 7027–7046, https://doi.org/10.1002/2017JD026494.

——, F. Zhang, E. E. Clothiaux, L. N. Zhang, and Y. Lu, 2018: Representing precipitation ice species with both spherical and nonspherical particles for radiative transfer modeling of microphysics-consistent cloud microwave scattering properties. *J. Adv. Model. Earth Syst.*, **10**, 1011–1028, https://doi.org/10.1002/2017MS001226.

Sippel, J. A., and F. Zhang, 2008: A probabilistic analysis of the dynamics and predictability of tropical cyclogenesis. *J. Atmos. Sci.*, **65**, 3440–3459, https://doi.org/10.1175/2008JAS2597.1.

——, and ——, 2010: Factors affecting the predictability of Hurricane Humberto (2007). *J. Atmos. Sci.*, **67**, 1759–1778, https://doi.org/10.1175/2010JAS3172.1.

——, S. A. Braun, and C.-L. Shie, 2011: Environmental influences on the strength of tropical Storm Debby (2006). *J. Atmos. Sci.*, **68**, 2557–2581, https://doi.org/10.1175/2011JAS3648.1.

Skamarock, W. C., and Coauthors, 2008: A description of the advanced research WRF version 3. NCAR Tech. Note NCAR/TN-475+STR, 125 pp., https://doi.org/10.5065/D68S4MVH.

Skofronick-Jackson, G., and Coauthors, 2017: The Global Precipitation Measurement (GPM) mission for science and society. *Bull. Amer. Meteor. Soc.*, **98**, 1679–1695, https://doi.org/10.1175/BAMS-D-15-00306.1.

Smith, R. K., and M. T. Montgomery, 2012: Observations of the convective environment in developing and non-developing tropical disturbances. *Quart. J. Roy. Meteor. Soc.*, **138**, 1721–1739, https://doi.org/10.1002/qj.1910.

Tang, B. H., and Coauthors, 2020: Recent advances in research on tropical cyclogenesis. *Trop. Cyclone Res. Rev.*, **9**, 87–105, https://doi.org/10.1016/j.tcrr.2020.04.004.

Tang, X., and F. Zhang, 2016: Impacts of the diurnal radiation cycle on the formation, intensity, and structure of Hurricane Edouard (2014). *J. Atmos. Sci.*, **73**, 2871–2892, https://doi.org/10.1175/JAS-D-15-0283.1.

Thompson, G., P. R. Field, R. M. Rasmussen, and W. D. Hall, 2008: Explicit forecasts of winter precipitation using an improved bulk microphysics scheme. Part II: Implementation of a new snow parameterization. *Mon. Wea. Rev.*, **136**, 5095–5115, https://doi.org/10.1175/2008MWR2387.1.

Torn, R. D., 2010: Ensemble-based sensitivity analysis applied to African easterly waves. *Wea. Forecasting*, **25**, 61–78, https://doi.org/10.1175/2009WAF2222255.1.

——, and D. Cook, 2013: The role of vortex and environment errors in genesis forecasts of Hurricanes Danielle and Karl (2010). *Mon. Wea. Rev.*, **141**, 232–251, https://doi.org/10.1175/MWR-D-12-00086.1.

Ventrice, M. J., C. D. Thorncroft, and M. A. Janiga, 2012a: Atlantic tropical cyclogenesis: A three-way interaction between an African easterly wave, diurnally varying convection, and a convectively coupled atmospheric Kelvin wave. *Mon. Wea. Rev.*, **140**, 1108–1124, https://doi.org/10.1175/MWR-D-11-00122.1.

——, ——, and C. J. Schreck III, 2012b: Impacts of convectively coupled Kelvin waves on environmental conditions for Atlantic tropical cyclogenesis. *Mon. Wea. Rev.*, **140**, 2198–2214, https://doi.org/10.1175/MWR-D-11-00305.1.

Wang, S., A. H. Sobel, F. Zhang, Y. Q. Sun, Y. Yue, and L. Zhou, 2015: Regional simulation of the October and November MJO events observed during the CINDY/DYNAMO field campaign at gray zone resolution. *J. Climate*, **28**, 2097–2119, https://doi.org/10.1175/JCLI-D-14-00294.1.

Wang, Z., M. T. Montgomery, and T. J. Dunkerton, 2010: Genesis of pre–Hurricane Felix (2007). Part I: The role of the easterly wave critical layer. *J. Atmos. Sci.*, **67**, 1711–1729, https://doi.org/10.1175/2009JAS3420.1.

Weng, F., 2007: Advances in radiative transfer modeling in support of satellite data assimilation. *J. Atmos. Sci.*, **64**, 3799–3807, https://doi.org/10.1175/2007JAS2112.1.

Weng, Y., and F. Zhang, 2012: Assimilating airborne Doppler radar observations with an ensemble Kalman filter for convection-permitting hurricane initialization and prediction: Katrina (2005). *Mon. Wea. Rev.*, **140**, 841–859, https://doi.org/10.1175/2011MWR3602.1.

——, and ——, 2016: Advances in convection-permitting tropical cyclone analysis and prediction through EnKF assimilation of reconnaissance aircraft observations. *J. Meteor. Soc. Japan*, **94**, 345–358, https://doi.org/10.2151/jmsj.2016-018.

Whitaker, J. S., and T. M. Hamill, 2002: Ensemble data assimilation without perturbed observations. *Mon. Wea. Rev.*, **130**, 1913–1924, https://doi.org/10.1175/1520-0493(2002)130<1913:EDAWPO>2.0.CO;2.

Wing, A. A., 2022: Acceleration of tropical cyclone development by cloud-radiative feedbacks. *J. Atmos. Sci.*, **79**, 2285–2305, https://doi.org/10.1175/JAS-D-21-0227.1.

Ying, Y., and F. Zhang, 2017: Practical and intrinsic predictability of multiscale weather and convectively coupled equatorial waves during the active phase of an MJO. *J. Atmos. Sci.*, **74**, 3771–3785, https://doi.org/10.1175/JAS-D-17-0157.1.

——, and ——, 2018: Potentials in improving predictability of multiscale tropical weather systems evaluated through ensemble assimilation of simulated satellite-based observations. *J. Atmos. Sci.*, **75**, 1675–1698, https://doi.org/10.1175/JAS-D-17-0245.1.

Zhang, F., and J. A. Sippel, 2009: Effects of moist convection on hurricane predictability. *J. Atmos. Sci.*, **66**, 1944–1961, https://doi.org/10.1175/2009JAS2824.1.

——, C. Snyder, and R. Rotunno, 2003: Effects of moist convection on mesoscale predictability. *J. Atmos. Sci.*, **60**, 1173–1185, https://doi.org/10.1175/1520-0469(2003)060<1173:EOMCOM>2.0.CO;2.

——, ——, and J. Sun, 2004: Impacts of initial estimate and observation availability on convective-scale data assimilation with an ensemble Kalman filter. *Mon. Wea. Rev.*, **132**, 1238–1253, https://doi.org/10.1175/1520-0493(2004)132<1238:IOIEAO>2.0.CO;2.

——, N. Bei, R. Rotunno, C. Snyder, and C. C. Epifanio, 2007: Mesoscale predictability of moist baroclinic waves: Convection-permitting experiments and multistage error growth dynamics. *J. Atmos. Sci.*, **64**, 3579–3594, https://doi.org/10.1175/JAS4028.1.

——, Y. Weng, J. A. Sippel, Z. Meng, and C. H. Bishop, 2009: Cloud-resolving hurricane initialization and prediction through assimilation of Doppler radar observations with an ensemble Kalman filter. *Mon. Wea. Rev.*, **137**, 2105–2125, https://doi.org/10.1175/2009MWR2645.1.

——, ——, J. F. Gamache, and F. D. Marks, 2011: Performance of convection-permitting hurricane initialization and prediction during 2008–2010 with ensemble data assimilation of inner-core airborne Doppler radar observations. *Geophys. Res. Lett.*, **38**, L15810, https://doi.org/10.1029/2011GL048469.

——, M. Minamide, and E. E. Clothiaux, 2016: Potential impacts of assimilating all-sky infrared satellite radiances from GOES-R on convection-permitting analysis and prediction of tropical cyclones. *Geophys. Res. Lett.*, **43**, 2954–2963, https://doi.org/10.1002/2016GL068468.

——, S. Taraphdar, and S. Wang, 2017: The role of global circumnavigating mode in the MJO initiation and propagation. *J. Geophys. Res. Atmos.*, **122**, 5837–5856, https://doi.org/10.1002/2016JD025665.

——, M. Minamide, R. G. Nystrom, X. Chen, S.-J. Lin, and L. M. Harris, 2019: Improving Harvey forecasts with next-generation weather satellites: Advanced hurricane analysis and prediction with assimilation of GOES-R all-sky radiances. *Bull. Amer. Meteor. Soc.*, **100**, 1217–1222, https://doi.org/10.1175/BAMS-D-18-0149.1.

Zhang, Y., and Coauthors, 2021: Ensemble-based assimilation of satellite all-sky microwave radiances improves intensity and rainfall predictions for Hurricane Harvey (2017). *Geophys. Res. Lett.*, **48**, e2021GL096410, https://doi.org/10.1029/2021GL096410.